Global Biogeochemical Cycles

RESEARCH ARTICLE

10.1029/2023GB007940

Special Section:
The U.S. GEOTRACES Pacific Meridional Transect (GP15)

Key Points:

- Settling speed of particulate organic carbon (POC) in the large size fraction increased with depth in the upper mesopelagic zone
- Settling flux of POC out of the euphotic zone was correlated with primary production, but the export efficiency was usually less than 5%
- Particles appeared to be more cohesive in low-productivity regions than in high-productivity regions

Supporting Information:

Supporting Information may be found in the online version of this article.

Correspondence to:

V. J. Amaral,
vamaral@ucsc.edu

Citation:

Amaral, V. J., Lam, P. J., Marchal, O., & Kenyon, J. A. (2024). Cycling rates of particulate organic carbon along the GEOTRACES Pacific meridional transect GP15. *Global Biogeochemical Cycles*, *38*, e2023GB007940. https://doi.org/10.1029/2023GB007940

Received 9 AUG 2023
Accepted 5 DEC 2023

Cycling Rates of Particulate Organic Carbon Along the GEOTRACES Pacific Meridional Transect GP15

Vinícius J. Amaral[1], Phoebe J. Lam[1], Olivier Marchal[2], and Jennifer A. Kenyon[3]

[1]Department of Ocean Sciences, University of California Santa Cruz, Santa Cruz, CA, USA, [2]Department of Geology and Geophysics, Woods Hole Oceanographic Institution, Woods Hole, MA, USA, [3]Department of Marine Chemistry and Geochemistry, Woods Hole Oceanographic Institution, Woods Hole, MA, USA

Abstract Understanding particle cycling processes in the ocean is critical for predicting the response of the biological carbon pump to external perturbations. Here, measurements of particulate organic carbon (POC) concentration in two size fractions (1–51 and >51 μm) from GEOTRACES Pacific meridional transect GP15 are combined with a POC cycling model to estimate rates of POC production, (dis)aggregation, sinking, remineralization, and vertical transport mediated by migrating zooplankton, in the euphotic zone (EZ) and upper mesopelagic zone (UMZ) of distinct environments. We find coherent variations in POC cycling parameters and fluxes throughout the transect. Thus, the settling speed of POC in the >51 μm fraction increased with depth in the UMZ, presumably due to higher particle densities at depth. The settling flux of total POC (>1 μm) out of the EZ was positively correlated with primary production integrated over the EZ; the highest export occurred in the subarctic gyre while the lowest occurred in the subtropical gyres. The ratio of POC settling flux to integrated primary production was low (<5%) along GP15, which suggests an efficient recycling of POC in the EZ in all trophic regimes. Specific rates of POC remineralization did not show clear variations with temperature or dissolved oxygen concentration, that is, POC recycling was apparently controlled by other factors such as microbial colonization and substrate lability. Particle cohesiveness, as approximated by the second-order rate constant for particle aggregation, was negatively correlated with trophic regime: particles appeared more cohesive in low-productivity regions than in high-productivity regions.

1. Introduction

The biological carbon pump is a network of processes that are responsible for fixing atmospheric carbon dioxide into organic biomass (i.e., particulate organic carbon, POC) in the surface ocean, cycling this organic carbon in the midwater, and eventually burying it at depth and in the sediment via export (Ducklow et al., 2001). While much attention has been given to quantifying how much carbon is exported from surface waters to the deep ocean, the processes that result in the cycling of carbon in the midwater and that are responsible for controlling carbon flux attenuation are relatively poorly understood. These processes include, for example, particle settling, aggregation, disaggregation, remineralization, and transport due to zooplankton diel vertical migration (DVM) (Iversen, 2023). Constraining the contributions of these individual processes is crucial for understanding how the biological carbon pump may respond to anthropogenic changes in ocean temperature and chemical composition (Yamamoto et al., 2018).

Quantifying the rates of particle settling, aggregation, disaggregation, remineralization, and DVM-mediated transport is notoriously difficult. Estimates of the rate constants that describe the kinetics of these processes are sparse. In a previous study, we combined measurements of size-fractionated POC concentration, prior estimates of rate constants derived from the literature, and other in-situ data, to derive particle cycling rates in the upper 500 m of the water column at Station P in the eastern north Pacific during the summer of 2018 (Amaral et al., 2022). Whilst this study provided insight into POC cycling at Station P, our posterior estimates of particle cycling rate constants were found to be largely dependent on prior estimates, and they may not be appropriate to describe POC cycling in other biogeochemical regimes.

The GEOTRACES Pacific meridional transect GP15 was conducted between 24 September 2018 through 22 November 2018. This transect includes stations within the Alaskan (subarctic) gyre, the transition zone chlorophyll front (Polovina et al., 2001), the north and south Pacific subtropical gyres, and the equatorial upwelling region (Figure 1). The various data sets collected at these stations provide an opportunity to examine how particle cycling parameters vary as a function of biogeochemical environment. In this study, we extend the work of

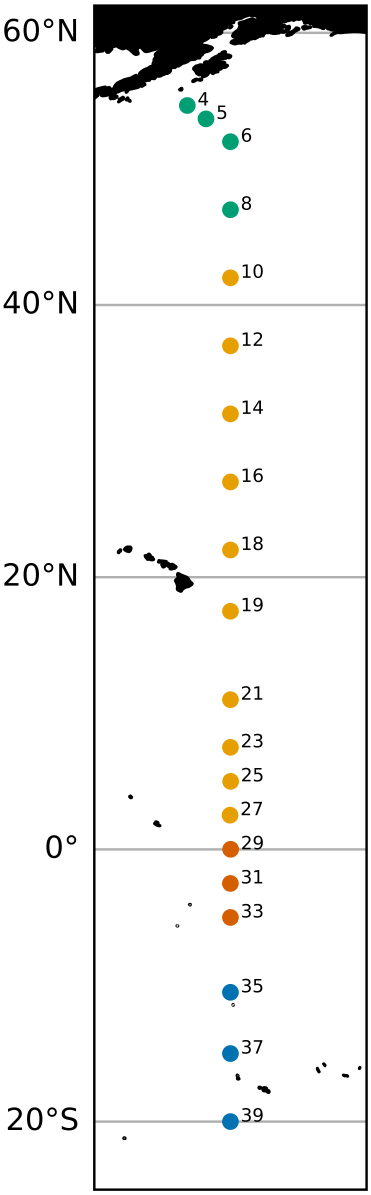

Figure 1. The GEOTRACES Pacific meridional transect GP15. Markers indicates station numbers. Most stations lie along 152°W. "Subarctic" stations are shown in green, "North Pacific gyre" stations in orange, "Equatorial" stations in red, and "South Pacific gyre" stations in blue. This classification is consistent with surface nutrient concentrations and a water mass analysis (Lawrence et al., 2022).

Amaral et al. (2022) by estimating particle cycling parameters and vertical carbon export in a wide range of oceanic environments across GP15. We examine relationships between environmental variables and particle cycling, with due consideration for the errors in the measurements and in prior estimates of particle cycling parameters. Emphasis is placed on (a) the influence of seawater viscosity on particle settling speed, (b) the effect of trophic regime and phytoplankton community composition on POC export by gravitational settling, (c) the influence of phytoplankton community composition on particle (dis)aggregation, and (d) the dependence of POC remineralization on temperature and dissolved oxygen concentration. Each of these effects is elaborated below.

According to Stokes' Law, the settling velocity of a rigid spherical particle in a fluid is proportional to its excess density relatively to the fluid and inversely proportional to the fluid viscosity. Thus, processes that increase the density of particles are expected to increase settling speed. An increase in particulate settling speed with depth has been inferred from measurements of vertical POC flux from sediment traps (Berelson, 2002), lead and polonium isotope concentrations (Villa-Alfageme et al., 2016), and particle composition (Xiang et al., 2022). One common explanation for this phenomenon is the preferential remineralization of labile particulate material near the surface (Nguyen et al., 2022), leaving behind denser refractory material such as biominerals and lithogenic particles to sink at depth (Xiang et al., 2022). In addition, particle settling speeds should increase as seawater viscosity decreases, that is, as seawater temperature increases (Millero, 1974). However, a relationship between particle settling speed and seawater temperature was not observed in laboratory experiments (Iversen & Ploug, 2013) or field studies (McDonnell et al., 2015; Trull et al., 2008). In this work, we estimate particle sinking speeds at relatively high vertical resolution across a range of seawater temperatures, which allows us to examine whether particle settling speeds vary with depth and/or seawater viscosity.

Particle settling speeds are important because they partly control the settling flux of POC out of the euphotic zone (EZ), and thus influence the strength of the biological pump. However, the settling flux of POC at the base of the EZ is also governed by the standing stock of POC in the EZ. Pelagic ecosystems characterized by higher primary production and phytoplankton communities dominated by microplankton (e.g., diatoms) are expected to show larger POC settling fluxes out of the EZ (Boyd & Newton, 1999; Guidi et al., 2009). Buesseler (1998) showed that the fraction of production that is exported by settling (i.e., the export efficiency) can be low throughout much of the ocean (<5%–10%), with mid- and high-latitude diatom blooms often characterized by higher export efficiency. Later work showed that regions where primary production is high and spatiotemporally variable may exhibit variable export efficiencies (Henson et al., 2015; Maiti et al., 2013), as may regions with dynamic zooplankton communities (Wassmann, 1998). In this study, we compare our estimates of POC export flux with concurrent estimates of primary production and phytoplankton community composition to evaluate whether these two variables affect the fraction of POC exported out of the EZ.

Phytoplankton community composition may also affect the rates at which particles (dis)aggregate. Whilst earlier models of marine particle aggregation assumed that particle aggregation is first-order with respect to particle concentration (e.g., Clegg & Whitfield, 1990; Murnane et al., 1990), more recent work has shown that particle aggregation is better described as a second-order process (e.g., Burd, 2013). In the second-order formulation of aggregation, the second-order rate constant is expected to reflect particle properties such as the cohesiveness of the interacting particles. Thus, aggregation rates should be higher in regions dominated by plankton that produce "stickier" aggregates and/or where particle concentrations are high (Iuculano et al., 2017; Passow, 2002; Wurl et al., 2011; Zamanillo et al., 2019). In contrast, regions where particulate matter is less cohesive and zooplankton activity (e.g., swimming) is more intense, may be characterized by relatively large rates of particle disaggregation (Briggs et al., 2020; Dilling & Alldredge, 2000). Zooplankton grazing may promote both the formation of particle aggregates (e.g., through the packaging of algal material into fecal pellets) and the destruction of such aggregates (e.g., via particle fragmentation during feeding). Here we examine how rate constants of particle (dis)aggregation vary as a function of phytoplankton community composition and zooplankton grazing rate in the EZ.

Finally, rates of POC remineralization may vary geographically and with depth owing to a dependence of microbial activity on temperature and dissolved O_2 concentration. Indeed, particles in surface waters are densely colonized by microbes, which may not efficiently mineralize organic material as the particles sink to colder temperatures, higher pressures, and lower dissolved O_2 concentrations (Iversen, 2023; Nguyen et al., 2022). Similarly, at a given depth, oceanic regions with warmer temperatures may be characterized by higher remineralization rates, as microbial respiration generally increases with temperature (Cram et al., 2018; Laufkötter et al., 2017; Marsay et al., 2015). In this study, we test these correlations by comparing our depth-dependent estimates of particle remineralization rate constants with measurements of temperature and dissolved O_2 concentration from CTD data.

The organization of this paper is as follows. First, in Section 2.1 we present the data used in this study. In Sections 2.2 and 2.3, we describe the model and the inverse method that are applied to infer particle cycling rates from POC concentration data from the upper water column along GP15. Prior knowledge of particle cycling processes is assembled in Section 2.4. Results from data inversions are presented in Section 3, and discussed in Section 4. Finally, we provide a summary in Section 5.

2. Methods

2.1. Data

This study relies on measurements of POC concentration collected in the upper 600 m at different stations along GP15. POC concentrations were measured from particle samples collected by large volume in-situ filtration (LVISF), and their errors were estimated from the standard deviation of process blank filters (Lam et al., 2015, 2018; Xiang & Lam, 2020). Quartz microfiber filters (1-μm nominal porosity) and polyester screens (51 μm) were used to separate particles into small (SSF) and large (LSF) size fractions, respectively (Figure 2 and Figure S1 in Supporting Information S1). For convenience, POC concentrations in the SSF and LSF are denoted as P_S and P_L, respectively. In total, there are 76 measurements of [POC] in the EZ and 60 measurements of [POC] in the upper mesopelagic zone (UMZ). For this study, the depth of the EZ is derived from the 1% light level (see Section 2.4). The closest sampling depth to the base of the EZ and all sampling depths above it are assumed to be within the EZ. All other sampling depths are assumed to be in the UMZ.

This study also relies on other types of measurements. We use vertical POC fluxes constrained from water column ^{234}Th concentrations and the POC/^{234}Th ratio of particles captured by LVISF (Buesseler, 2021a, 2021b). Particulate ^{234}Th activities were measured from the same filters used for POC analysis, while water column ^{234}Th concentrations were measured on bottle samples closest to the LVISF sampling depths (Kenyon, 2022). Pigment samples were collected in the EZ on GF/F filters and analyzed by high-performance liquid chromatography at Oregon State University (Cutter et al., 2023a, 2023b; Latasa et al., 1996). Phytoplanktonic fractions are calculated following Uitz et al. (2006) using averages of different pigment concentrations in the EZ. They correspond to picoplankton (<2 μm; cyanobacteria, prochlorophytes, and green flagellates), nanoplankton (2–20 μm; chromophytes, nanoflagellates, and cryptophytes), and microplankton (>20 μm; diatoms and dinoflagellates) (Vidussi et al., 2001). Temperature, salinity, and dissolved O_2 concentrations were measured by sensors mounted on the CTD rosette, and sensor O_2 data were verified by Winkler titration (Casciotti et al., 2019; Cutter et al., 2019). Nitrate, silicate, and phosphate concentrations were measured on bottle samples also collected on the CTD rosette (Casciotti et al., 2021a, 2021b). The mixed layer depths at GP15 stations are based on a 0.05 kg m^{-3} density difference from the surface water (Bishop et al., 2022). Over the entire transect, 8-day averages of the diffuse attenuation coefficient (K_d) were derived at 4-km resolution from the NASA Aqua MODIS sensor (Acker & Leptoukh, 2007; NASA Ocean Biology Processing Group, 2018). For a given station, we use the 8-day averaging interval that includes the sampling time of the shallowest LVISF cast.

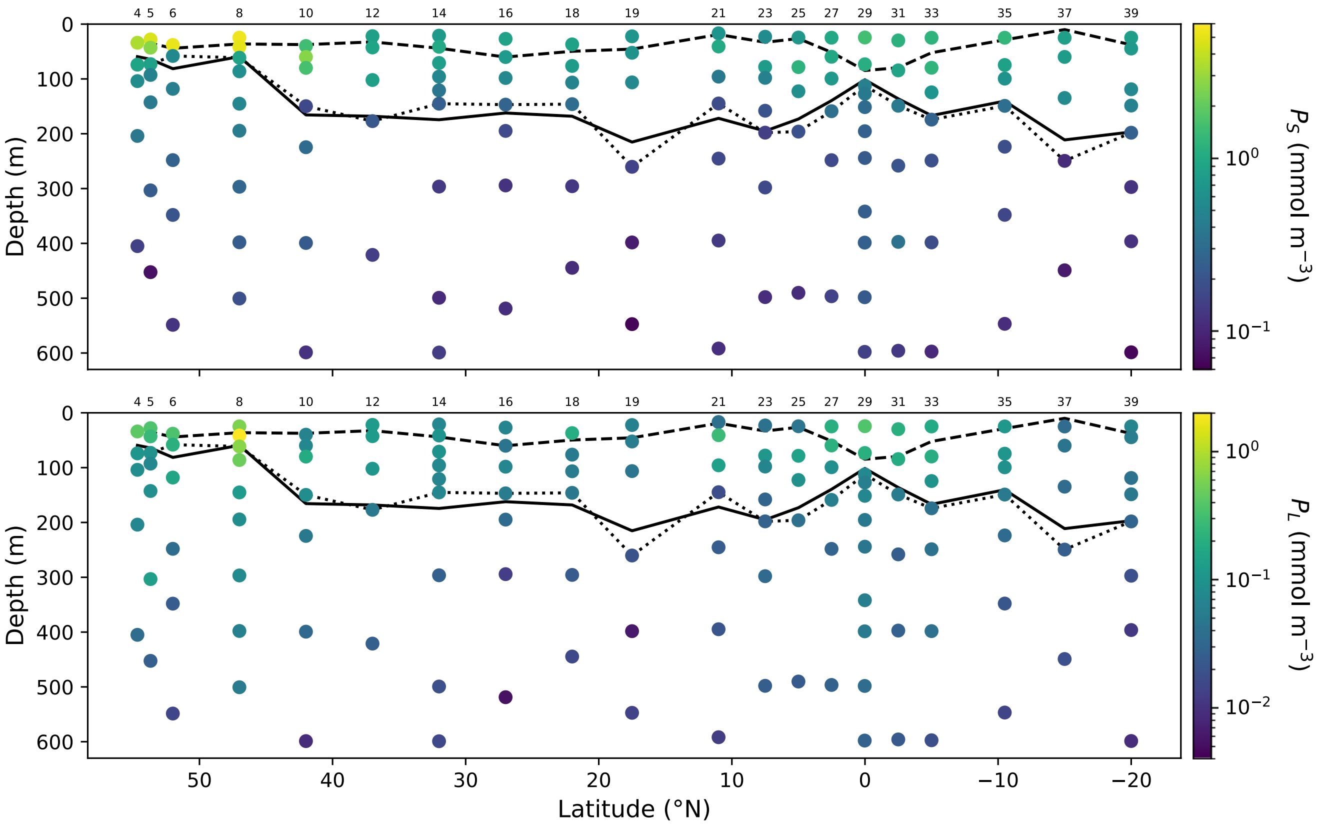

Figure 2. Sections of particulate organic carbon concentration measured during GP15 in the small size fraction (1–51 μm; top panel) and the large size fraction (>51 μm; bottom panel). Dashed line shows the mixed layer depth, solid line shows the depth of the euphotic zone, and dotted line shows the depth of the zooplankton grazing zone.

2.2. Model

We use a POC cycling model with two particle size classes, which is described in Amaral et al. (2022) and is summarized in Figure 3. Consideration of two size classes allows us to make inferences about particle aggregation and disaggregation rates, as well as about particle remineralization and settling rates in the two size fractions (1–51 and >51 μm). The model domain extends from the sea surface to the depth of the deepest sample in the upper 600 m of the water column. Since the depth of the deepest sample in the upper 600 m varies between stations, the model domain also varies between stations. The water column is represented by different layers. The upper and lower boundaries of each layer coincide with the depth of samples obtained from LVISF, except for the upper boundary of the uppermost layer, which coincides with the sea surface.

The balance equations that describe the cycling of POC in the SSF and LSF in a given layer, are, respectively:

$$-\left(w_S^b P_S^b - w_S^t P_S^t\right) + \int_{z_t}^{z_b} \dot{P}_S \, dz + \beta_{-2}\overline{P_L}h - \left(\beta_2'\overline{P_S} + \beta_{-1,S}\right)\overline{P_S}h - \beta_3\overline{P_S}\int_{z_t}^{z_b} H(z_g - z)\, dz = 0 \tag{1a}$$

$$-\left(w_L^b P_L^b - w_L^t P_L^t\right) + \beta_2'\overline{P_S}^2 h - (\beta_{-2} + \beta_{-1,L})\overline{P_L}h + \beta_3\overline{P_S}^g \int_{z_t}^{z_b} E(z)\, dz = 0 \tag{1b}$$

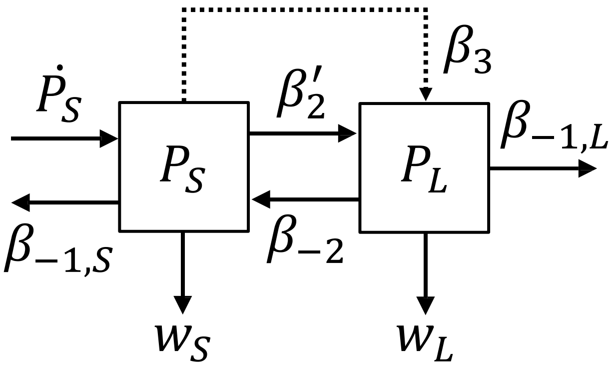

Figure 3. Schematic of the particulate organic carbon (POC) cycling model. Small POC (P_S) is produced from primary production ($\dot{P}_S$) and when large POC disaggregates (β_{-2}), and it is removed when P_S aggregates (β_2'), remineralizes ($\beta_{-1,S}$), and is consumed by zooplankton (β_3). Large POC (P_L) is produced when P_S aggregates or is egested by zooplankton (β_3), and it is removed when it disaggregates and remineralizes ($\beta_{-1,L}$). Both P_S and P_L sink through the water column (w_S and w_L). The dashed line labeled with β_3 serves to indicate that zooplankton consume P_S only in the euphotic zone and egest P_L only in the upper mesopelagic zone.

Here, P_S is [POC] in the SSF, P_L is [POC] in the LSF, $\dot{P}_S$ is the primary production of P_S, w_S is the settling speed of P_S, w_L is the settling speed of P_L, $\beta_{-1,S}$ is the rate constant for remineralization of P_S, $\beta_{-1,L}$ is the rate constant for remineralization of P_L, β_2' is the rate constant for P_S aggregation, β_{-2} is the rate constant for P_L disaggregation, and β_3 is the rate constant for ingestion of P_S by vertically migrating zooplankton in the grazing zone.The depth z_t is the depth at the top of the layer, z_b is the depth at the bottom of the layer, $h = z_b - z_t$ is the thickness of the layer, and an overbar denotes an average over the layer. Specifically, $\overline{P_S}$ and $\overline{P_L}$ are calculated from the arithmetic mean of their respective concentrations at the two layer boundaries, except for the surface layer, where they are set to the concentrations at the base of that layer. At the sea surface, the settling fluxes $w_S^t P_S^t$ and $w_L^t P_L^t$ are assumed to vanish. The function H is a Heaviside function ($H(z_g - z) = 1$ if $z < z_g$ and $H(z_g - z) = 0$ otherwise, where z_g is the depth of the grazing zone and z is the depth), $E(z)$ is a function representing the vertical distribution of zooplankton egestion in the UMZ, and $\overline{P}_S^g$ is the average P_S concentration in the grazing zone. In this study, the depth of the grazing zone, z_g, is set equal to the pump depth closest to the base of the EZ, z_{EZ}. Also, "remineralization" includes any transfer of organic carbon from the particulate phase to the organic and inorganic "dissolved" phases, operationally defined as the material that passes through the 1 μm filter. All processes that transfer POC between size fractions are assumed to be first-order with respect to POC concentration, except for aggregation (β_2'), which is assumed to be second order (Amaral et al., 2022; Jackson & Burd, 2015).

Equation 1a states that the sources of P_S from particle production and large particle disaggregation should be balanced by the divergence of the SSF settling flux and by the sinks from small particle remineralization, aggregation, and zooplankton ingestion (in the grazing zone). Likewise, Equation 1b states that the sources of P_L from small particle aggregation and zooplankton egestion (below the grazing zone) should be balanced by the divergence of the LSF settling flux and by the sinks from large particle remineralization and disaggregation. Note that primary production is assumed to be a source of POC in the SSF but not in the LSF.

Primary production of P_S ($\dot{P}_S$) is assumed to decrease exponentially with depth,

$$\dot{P}_S = \dot{P}_{S,0} \exp\left\{-\frac{z}{L_P}\right\} \tag{2}$$

where $\dot{P}_{S,0}$ is the production at the surface and L_P is a vertical scale.

Zooplankton export POC from surface waters to the deep ocean via DVM. We assume that zooplankton consume POC in the SSF and egest it to the LSF to represent the packaging of small algal particles into larger fecal pellets. We also assume that grazing occurs above z_g (i.e., in the EZ), where zooplankton feed at night, and that egestion occurs only below z_g (i.e., in the UMZ), where zooplankton reside during the day. In Equation 1b, $\beta_3 \overline{P}_S^g$ is the average P_S ingestion rate from the surface to z_g and $\overline{P}_S^g$ is

$$\overline{P}_S^g = \frac{1}{z_g} \int_0^{z_g} P_S(z)\, dz \tag{3}$$

We parameterize DVM in a way that reflects a subsurface maximum in daytime zooplankton biomass observed by Omand et al. (2021). To model the egestion rate, we multiply $\beta_3 \overline{P}_S^g$ by the layer integral of the dimensionless function $E(z)$:

$$E(z) = E_{\max} \sin\left(\frac{\pi\left[z - z_g\right]}{z_m - z_g}\right) H(z - z_g) \tag{4}$$

Here, $E_{\max}$ is the maximum value of the egestion function $E(z)$ and occurs at the middepth between z_m (maximum depth of zooplankton migration) and z_g (depth of the grazing zone). It is determined from a metabolic constraint that sets the vertical integral of the egestion flux in the UMZ to be a fraction, α, of the vertical integral of the ingestion flux in the grazing zone (between 0 and z_g), such that

$$E_{\max} = \frac{\pi \alpha z_g}{2(z_m - z_g)} \tag{5}$$

The Heaviside function in Equation 4 implies that $E(z) = H(z - z_g) = 0$ at depths where $z < z_g$, which reflects our assumption that no POC egestion occurs above z_g.

The integrals in Equations 1a and 1b are:

$$\int_{z_t}^{z_b} \dot{P}_S \, dz = \dot{P}_{S,0} L_P \left(\exp\left\{ -\frac{z_t}{L_P} \right\} - \exp\left\{ -\frac{z_b}{L_P} \right\} \right) \tag{6a}$$

$$\int_{z_t}^{z_b} H(z_g - z) \, dz = \begin{cases} h & z_b < z_g \\ 0 & z_t > z_g \end{cases} \tag{6b}$$

$$\int_{z_t}^{z_b} E(z) \, dz = \begin{cases} 0 & z_b < z_g \\ E_{max} \frac{z_m - z_g}{\pi} \left[\cos\left(\frac{\pi [z_t - z_g]}{z_m - z_g} \right) - \cos\left(\frac{\pi [z_b - z_g]}{z_m - z_g} \right) \right] & z_t > z_g \end{cases} \tag{6c}$$

Finally, we include an additional equation for every layer boundary, which states that the sum of settling fluxes in the small and large size fractions ($w_S P_S$ and $w_L P_L$, respectively) is equal to the settling flux as estimated from ^{234}Th (F_{Th}):

$$F_{Th} - (w_S P_S + w_L P_L) = 0 \tag{7}$$

In summary, the POC cycling model includes 11 parameters (w_S, w_L, $\beta_{-1,S}$, $\beta_{-1,L}$, β_2', β_{-2}, $\dot{P}_{S,0}$, L_P, β_3, α, z_m). The rate constants $\beta_{-1,S}$, $\beta_{-1,L}$, β_2', and β_{-2} are assumed to be uniform within each layer, but are allowed to vary between layers. The particle settling speeds w_S and w_L are defined at the layer boundaries and are allowed to vary between layer boundaries. The other parameters, $\dot{P}_{S,0}$, L_P, β_3, α, and z_m, take on a single value at a given station.

2.3. Inverse Method

An inverse method is used to estimate the particle cycling parameters of the model (Section 2.2) from the size-fractionated measurements of POC concentration, estimates of vertical POC settling flux based on ^{234}Th, and other observations along GP15 (Section 2.1). A complete description of this method can be found in Amaral et al. (2022). Briefly, the model parameters, the POC concentrations (P_S and P_L), and the POC settling flux from ^{234}Th (F_{Th}) at a given station are defined as variables in a state vector, $\boldsymbol{x}$. Equations 1a, 1b, and 7 are assembled in a single equation $\boldsymbol{f}(\boldsymbol{x}) = \boldsymbol{0}$, where $\boldsymbol{f}(\boldsymbol{x})$ is a vector of functions and $\boldsymbol{0}$ is a vector of zeros. We use the algorithm of total inversion (ATI) (Tarantola & Valette, 1982) to find an estimate of the state vector $\boldsymbol{x}$ that minimizes the cost function

$$J = (\boldsymbol{x} - \boldsymbol{x}_o)^T \boldsymbol{C}_o^{-1} (\boldsymbol{x} - \boldsymbol{x}_o) \quad \text{subject to} \quad \boldsymbol{f}(\boldsymbol{x}) = \boldsymbol{0} \tag{8}$$

where superscript T denotes the transpose. Here, $\boldsymbol{x}_o$ is a vector that includes prior estimates of the elements of $\boldsymbol{x}$ and $\boldsymbol{C}_o$ is the error covariance matrix, or uncertainty, for the prior values in $\boldsymbol{x}_o$. The diagonal elements of $\boldsymbol{C}_o$ are the squares of the uncertainties in the prior estimates in $\boldsymbol{x}_o$ and the off-diagonal elements of $\boldsymbol{C}_o$ are the covariances between these uncertainties. As error covariances are poorly constrained, all off-diagonal elements in $\boldsymbol{C}_o$ are set to zero in this study.

Note that in Amaral et al. (2022), Equations 1a and 1b included error terms to account for the expectation that these balance equations do not consider all processes that may affect the distribution of POC in the water column, such as lateral and vertical transport. However, we found in this previous work that the ATI tended to adjust the posterior estimates of these error terms rather than the particle cycling parameters in order to satisfy the balance equations, which prevented the posterior estimates of the cycling parameters from varying noticeably relatively to their prior estimates. In this study, we do not include error terms in Equations 1a and 1b, that is, these equations are assumed to be exact when inferring values of POC concentrations and rate parameters.

2.4. Prior Knowledge

The inverse method applied in this study allows consideration of prior knowledge ($\boldsymbol{x}_o$) and prior uncertainties ($\boldsymbol{C}_o$) in the estimation of particle cycling parameters. Prior estimates of the state elements and their uncertainties are obtained from field measurements or from the literature (Table 1). Prior estimates of P_S and P_L and their uncertainties are based on measurements on LVISF samples and on their corresponding blank filters as described

Table 1
Variables and Parameters of the Particulate Organic Carbon (POC) Cycling Model

Symbol	Definition	Prior estimate	Prior error	Units	Reference
P_S, P_L	[POC] in SSF and LSF	Variable	Variable	mmol m^{-3}	This study
F_{Th}	POC settling flux from ^{234}Th	Variable	100%	mmol m^{-2} d^{-1}	This study
$\dot{P}_{S.0}$	Particle production at the surface	Variable	50%	mmol m^{-3} d^{-1}	Acker and Leptoukh (2007), NASA Ocean Biology Processing Group (2018), and Westberry et al. (2008)
L_P	Vertical scale for particle production	Variable	50%	m	NASA Ocean Biology Processing Group (2018) and Westberry et al. (2008)
β'_2	Second-order aggregation r.c.	0.00013–0.22	100%	m^3 $mmol^{-1}$ d^{-1}	Clegg et al. (1991), Murnane et al. (1994), and Murnane et al. (1996)
β_{-2}	Disaggregation r.c.	0.044–5.5	100%	d^{-1}	Clegg et al. (1991), Murnane et al. (1994, 1996), and Briggs et al. (2020)
$\beta_{-1,S}$	Remineralization r.c. (SSF)	0.0025–0.31	100%	d^{-1}	Clegg et al. (1991), Murnane et al. (1994), and Murnane et al. (1996)
$\beta_{-1,L}$	Remineralization r.c. (LSF)	0.012–0.43	100%	d^{-1}	Paul et al. (2022)
w_S	Particle settling speed (SSF)	0.045–1.8	100%	m d^{-1}	Krishnaswami et al. (1976, 1981), Rutgers van der Loeff and Berger (1993), Scholten et al. (1995), Venchiarutti et al. (2008), R. F. Anderson et al. (2016), Lerner et al. (2017), Gdaniec et al. (2020), and Xiang et al. (2022)
w_L	Particle settling speed (LSF)	2.5–130	100%	m d^{-1}	Murnane et al. (1996), Xiang et al. (2022), McDonnell and Buesseler (2010), McDonnell and Buesseler (2012), and McDonnell et al. (2015)
β_3	Zooplankton ingestion r.c.	Variable	50%	d^{-1}	Westberry et al. (2008), and Calbet (2001)
α	Zooplankton egestion fraction	0.30	50%	Unitless	Steinberg and Landry (2017)
z_m	Maximum depth of zooplankton migration	500	50%	m	Omand et al. (2021)

Note. r.c., rate constant.

in Section 2.1. If a sample is suspected to present an erroneous concentration due to collection and/or analysis issues, its concentration is instead obtained by linear interpolation of the concentrations immediately above and below the sample's depth (such interpolated values occur at only 5% of sampling depths). Prior estimates of the settling flux of total POC are obtained from ^{234}Th disequilibria (F_{Th}; Section 2.1) and are assumed to suffer from a relative error of 100%.

Prior estimates of the vertical scale of particle production (L_P) are obtained from satellite-derived estimates of the diffuse attenuation coefficient (K_d; Section 2.1). The estimate of L_P at a given station is taken as the reciprocal of the nearest available K_d estimate within the selected averaging interval. Albeit crude, this approach is consistent with the notion that the decrease of primary production with depth is driven primarily by light attenuation.

Next, consider $\dot{P}_{S.0}$. Integrating the primary production rate (Equation 2) from the surface to the base of the EZ (z_{EZ}) yields:

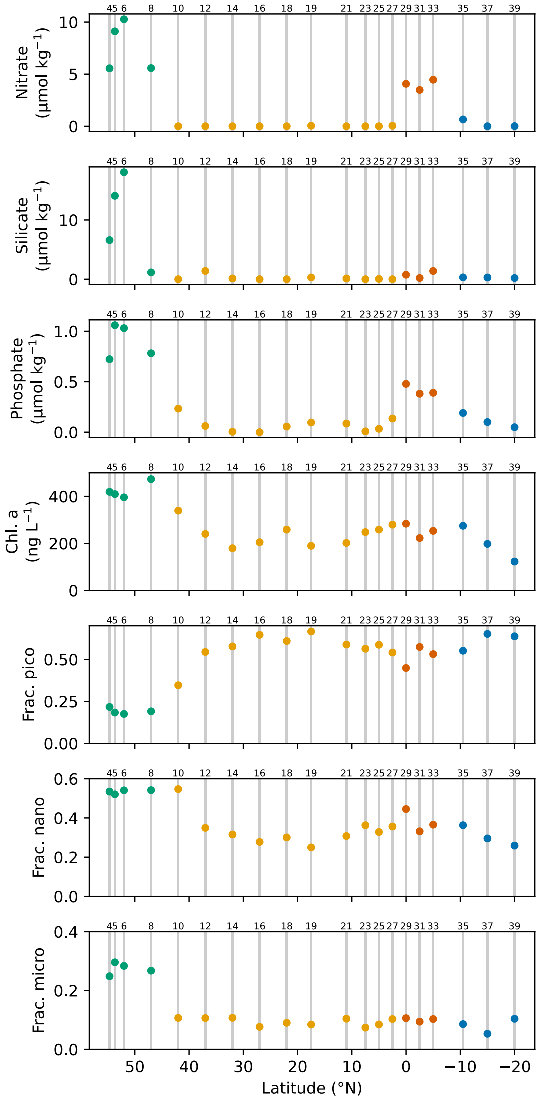

Figure 4. Nutrient concentrations, chlorophyll a (Chl. a) concentrations, and fractions of different size classes in the phytoplankton assemblages across GP15. Nutrient concentrations are averages over the mixed layer. Chl. a concentrations and phytoplankton fractions are averages over the euphotic zone. "Subarctic" stations are shown in green, "North Pacific gyre" stations in orange, "Equatorial" stations in red, and "South Pacific gyre" stations in blue (Figure 1). Gray vertical bars in each panel connect the latitudes to the station numbers above each panel.

$$\int_0^{z_{EZ}} \dot{P}_S \, dz = \dot{P}_{S,0} L_P \left(1 - \exp\left\{-\frac{z_{EZ}}{L_P}\right\}\right) \tag{9}$$

The base of the EZ, z_{EZ}, is taken as the 1% light level. With z_{EZ} estimated from $\frac{1}{K_d} \cdot \ln(100) = L_P \cdot \ln(100)$, Equation 9 yields:

$$\dot{P}_{S,0} = \frac{\int_0^{z_{EZ}} \dot{P}_S \, dz}{L_P \cdot 0.99} \tag{10}$$

The vertical integral of the primary production rate (numerator in Equation 10) is approximated from chlorophyll concentration data measured from satellites and the Carbon-based Production Model (Westberry et al., 2008). Like for L_P, for a given station, we select the integrated production rate for the 8-day averaging interval that includes the sampling time of the shallowest pump cast. The nearest-in-time estimates of integrated primary production rate and L_P are then used to calculate a prior estimate of $\dot{P}_{S,0}$ using Equation 10.

Prior information about parameters related to DVM is obtained as follows. For each station, the zooplankton ingestion rate constant (β_3) is estimated from the depth-integrated primary production estimated at that station and an empirical relationship between primary production and biomass-specific ingestion rate (Calbet, 2001, their Figure 2). Zooplankton are estimated to use approximately 70% of their food for growth and metabolism (Steinberg & Landry, 2017). Accordingly, the prior value of the egestion fraction, α, is set equal to 30%. Finally, the prior estimate of the maximum zooplankton migration depth (z_m) is set to 500 m, which is about the depth where a maximum in daytime zooplankton biomass was observed near Station P (Omand et al., 2021).

Prior estimates of the remaining particle cycling parameters (w_S, w_L, $\beta_{-1,S}$, $\beta_{-1,L}$, β_2', β_{-2}) vary over a wide range (see Table 1), and we previously found a strong dependence of posterior estimates on prior estimates (Amaral et al., 2022). To address these issues, we perform a total of 10^5 inversions, each with a different set of parameter values selected randomly ("Monte Carlo" approach). First, parameter estimates from the upper 600 m are compiled from the literature and outliers are removed via the interquartile method. Specifically, for a given parameter, we discard estimates that lie outside the range defined by (a) the first quartile of the compiled values minus 1.5 times the interquartile range and (b) the third quartile plus the 1.5 times the interquartile range. The minimum and maximum of the remaining set define a uniform distribution from which prior estimates are chosen randomly. As no prior estimates of β_2' exist in the literature to our knowledge, we define ranges for this parameter by dividing prior estimates of the first-order aggregation constant by the median of the P_S concentration data considered in this study (0.38 mmol m^{-3}). Prior errors of $\dot{P}_{S,0}$, L_P, β_3, α, and z_m are not available in the literature, and we assume a relative error of 50% for these parameters.

3. Results

3.1. Hydrographic Context

In this section, we describe how nutrient and chlorophyll concentrations, phytoplankton community composition, temperature, and dissolved O_2 concentration vary along GP15 (Figure 4). Nitrate, phosphate, and silicate concentrations in the mixed layer are relatively high in the subarctic Pacific and are depleted in the subtropical gyres.

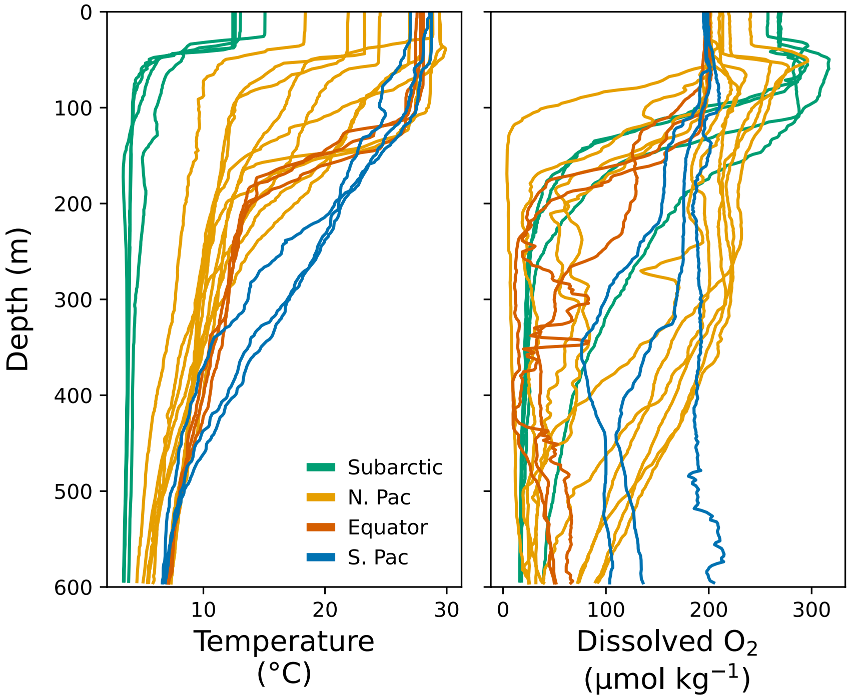

Figure 5. Vertical profiles of temperature and dissolved O_2 concentration measured from CTD sensors. The profiles are colored according to the different biogeochemical environments sampled during GP15 (Figure 1).

Near the equator, nitrate and phosphate levels are notably elevated, while silicate levels exhibit only slightly higher values in comparison to the subtropical gyres. The average concentration of chlorophyll a (Chl. a) in the EZ is also highest in the subarctic Pacific and decreases southward along the section until about 30°N. Chl. a shows some variation throughout the rest of the transect and presents secondary maxima near the equator. North of 45°N (i.e., the subarctic Pacific), the phytoplankton assemblage is dominated by nanoplankton (>50%) and microplankton (~25%–30%). South of 45°N, the phytoplankton assemblage is dominated by picoplankton and nanoplankton, together accounting for 90% or more of the algal community. From 45° to 25°N, the relative abundance of nanoplankton decreases from roughly 55%–30%, while the relative abundance of picoplankton increases from approximately 30%–60%. Picoplankton remain dominant in the subtropical gyres, whilst the fraction of nanoplankton increases near the equator.

Temperature and dissolved O_2 concentration display large variations along GP15, which provides an opportunity to test the influence of these parameters on particle cycling. Temperatures at the surface are lowest in the subarctic Pacific, and generally increase southward along the section (Figure 5). In contrast, dissolved O_2 concentrations in surface waters decrease from north to south due to the temperature-dependent solubility of the gas in seawater. The wide range in temperature (15–20 °C) and O_2 concentration (0–200 μmol kg^{-1}) in the UMZ largely reflects the influence of different water masses along the transect (Lawrence et al., 2022). Many stations sampled the low oxygen waters of the North Pacific. Only one station (Station 21 at 11°N), located at the western extent of the eastern Tropical North Pacific oxygen deficient zone, had O_2 concentrations below the 2 μmol kg^{-1} detection limit of the CTD O_2 sensor.

3.2. Data Inversion

In this section, the parameters of the POC cycling model (Section 2.2) are estimated at different depths and at different stations along GP15 from size-fractionated POC measurements and other observations (Section 2.1) using the inverse method (Section 2.3).

First, we describe the POC concentration data that are inverted. Throughout the transect, the SSF dominates total POC and is usually an order of magnitude greater than the LSF (Figure 2 and Figure S1 in Supporting Information S1). In both size fractions, concentrations are typically highest at the surface and attenuate sharply

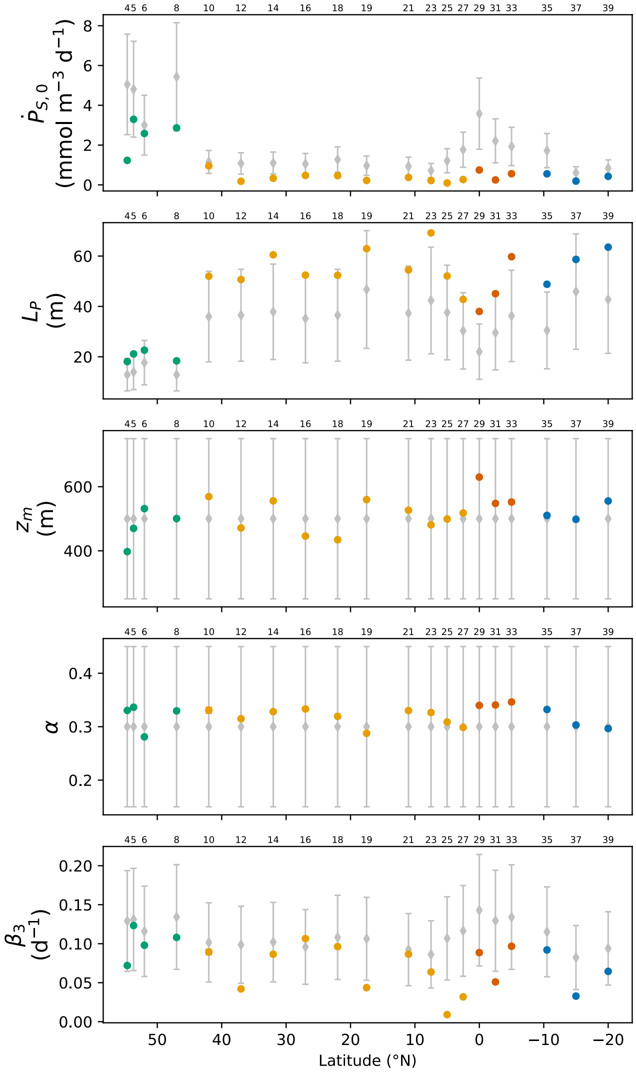

Figure 6. Estimates of particle production at the surface $\dot{P}_{S,0}$, vertical scale of particle production L_P, maximum depth of zooplankton migration z_m, zooplankton egestion fraction α, and zooplankton ingestion rate β_3, along GP15. Gray diamonds with vertical bars show prior estimates with their respective uncertainties (Table 1). Circles show mean posterior estimates and are color coded by biogeochemical regime (Figure 1). Error bars drawn to show standard errors of mean posterior estimates are usually too small to notice. Station numbers appear above each panel.

with depth. Concentrations are also highest in the subarctic gyre and lowest in the subtropical gyres. The mean of P_S throughout the transect in the EZ is 0.98 mmol m^{-3} with a standard deviation of 1.11 mmol m^{-3} and a range of 5.21 mmol m^{-3}. The mean of P_S in the UMZ is 0.21 mmol m^{-3} with a standard deviation of 0.12 mmol m^{-3} and a range of 0.52 mmol m^{-3}. The mean of P_L in the EZ is 0.14 mmol m^{-3} with a standard deviation of 0.24 mmol m^{-3} and a range of 1.92 mmol m^{-3}. The mean of P_L in the UMZ is 0.05 mmol m^{-3} with a standard deviation of 0.07 mmol m^{-3} and a range of 0.49 mmol m^{-3}.

The reported estimates of particle cycling parameters at a given station are means from all inversions that led to a converging solution of the inverse problem for that station (Section 2.3). Figure 6 shows prior and posterior estimates of particle cycling parameters with no depth dependence: the particle production at the surface ($\dot{P}_{S,0}$), the vertical scale of attenuation for particle production (L_P), and the three parameters that govern the effect of DVM on POC cycling, that is, the maximum depth of zooplankton grazing (z_m), the fraction of ingested carbon that is egested at depth (α), and the rate constant for zooplankton grazing in the grazing zone (β_3).

We find that the posterior estimates of the particle cycling parameters with no depth dependence are generally consistent with the prior estimates given the prior uncertainties (Figure 6). Interestingly, $\dot{P}_{S,0}$ values derived by inversion are usually lower than prior estimates, which may be due to undersampling of picoplankton by the nominal 1 μm pore size of QMA filters used to collect particles in the SSF (Amaral et al., 2022). This undersampling may also explain why L_P is usually overestimated, as suggested by the following argument. Higher particle concentrations are expected to lead to greater attenuation of light (i.e., greater K_d and shorter L_P). If pumps under-collect small particles, inversions of pump-collected POC data should lead to lower estimates of K_d and higher estimates of L_P. On the other hand, the latitudinal gradients in the prior estimates of K_d and L_P are reproduced by the posterior estimates. One caveat worth mentioning is that while we assume a prior estimate of 500 m for the maximum depth of zooplankton migration, z_m, at all stations, a value around 800–900 m may be more appropriate in the subtropical gyres (Steinberg et al., 2008). Nevertheless, Figure 6 shows that posterior estimates of z_m are not systematically larger at subtropical gyre stations, suggesting that this parameter may not be well constrained by the data used in our inversions.

Processes of particle aggregation, disaggregation, remineralization, and settling are also likely to influence the distribution of POC in the upper ocean (e.g., Amaral et al., 2022). The horizontal and vertical distributions of the parameters describing these processes are presented in Figure 7 and Figure S2 in Supporting Information S1. We find that the second-order rate constant for particle aggregation, β_2', is generally lower in surface subarctic Pacific waters compared to other locations. At stations south of 40°N, β_2' exhibits a subtle subsurface minimum between the mixed layer and the base of the EZ. We calculate the first-order aggregation rate constant as the product of the posterior values of β_2' and P_S, the concentration of POC in the SSF. Like P_S, the first-order aggregation rate constant, $\beta_2 = \beta_2' P_S$, is largest in the subarctic Pacific and smallest in the subtropical gyres, which reflects the lower P_S in subtropical regions. Similarly, our estimates of β_2 tend to decrease with depth along GP15 due to the vertical attenuation of P_S.

Our estimates of the rate constant for particle disaggregation, β_{-2}, are largest in the surface subarctic Pacific (Figure 7 and Figure S2 in Supporting Information S1). They tend to decrease with depth throughout the transect, but exhibit subsurface maxima in the lower EZ at some stations in the subtropical gyres and near the equator. The rate constant ratio β_{-2}/β_2 always exceeds 1, showing that the kinetics of particle disaggregation are faster than those of particle aggregation. The ratio is quite variable along GP15, but generally increases with depth, reflecting the increasing importance of disaggregation kinetics compared to aggregation kinetics due to the strong decrease of β_2 with depth.

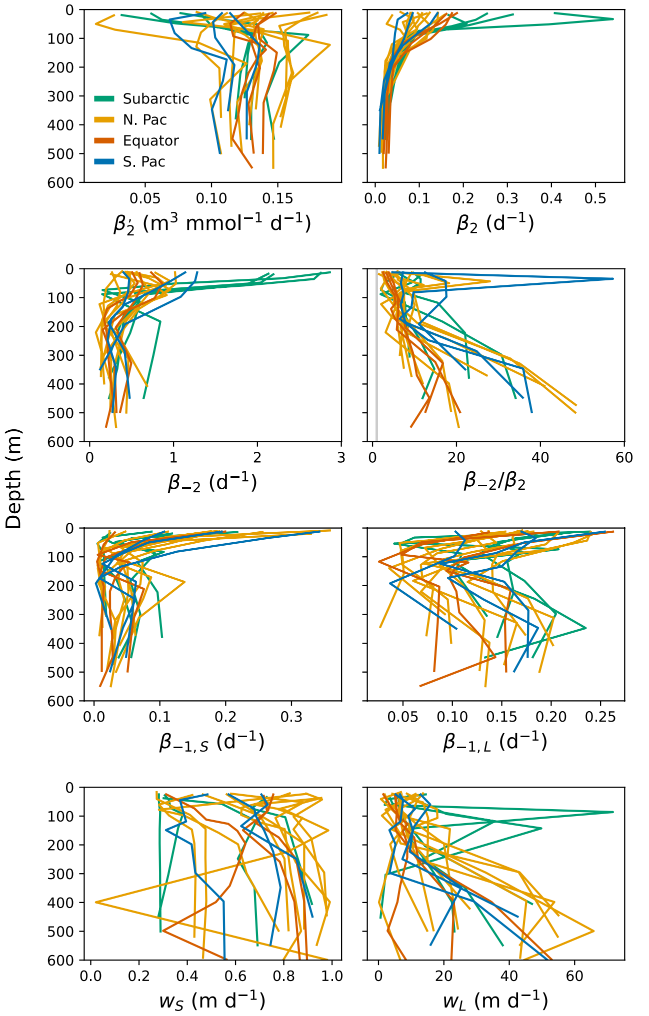

Figure 7. Profiles of second- and first-order aggregation rate constants (β_2' and β_2, respectively), disaggregation rate constant (β_{-2}), ratio of disaggregation to aggregation rate constants (β_{-2}/β_2), remineralization rate constants for the SSF and LSF ($\beta_{-1,S}$ and $\beta_{-1,L}$, respectively), and settling speed of the SSF and LSF (w_S and w_L, respectively). The estimates of β_2', β_2, β_{-2}, β_{-2}/β_2, $\beta_{-1,S}$, and $\beta_{-1,L}$ occur at the mid-depths of model layers, while the estimates w_S and w_L occur at layer boundaries. Each displayed value represents an average of the posterior estimates at a given station and at a given depth.

Particle remineralization is expected to contribute significantly to the decrease of POC with depth in the upper ocean. Our estimates of $\beta_{-1,S}$ tend to decrease downwards within the EZ throughout the transect, and are usually highest in the surface waters of the subtropical gyres (Figure 7 and Figure S2 in Supporting Information S1). The downward decrease of $\beta_{-1,S}$ in the EZ is generally much sharper in the subtropical gyres compared to subarctic and equatorial waters. At some stations, particularly in the subtropical gyres, $\beta_{-1,S}$ increases to a small local maximum in the UMZ between 150 and 300 m. Estimates of $\beta_{-1,L}$ are highly variable, and exhibit subsurface minima in the lower EZ between 100 and 200 m at many stations. Below these minima, $\beta_{-1,L}$ often increases to values comparable to those estimated at the surface at a given station.

While particle settling is key to the ocean biological pump, particle settling speeds in marine environments are difficult to estimate. Our estimates of w_S generally range from 0.2 to 1 m d^{-1} and usually show little depth variation at a given station (Figure 7 and Figure S2 in Supporting Information S1). Estimates of w_L are less than 20 m d^{-1} at the surface and show noticeable variations below the base of the EZ. In subarctic waters, we infer sharp maxima of w_L below the EZ between 100 and 200 m. Interestingly, south of the subarctic Pacific, estimates of w_L tend to increase with depth below the EZ (especially in the center of the subtropical gyres), reaching a maximum of 66 m d^{-1} at 499 m at Station 14.

4. Discussion

In this section, the lateral and vertical variations in our estimates of POC cycling rate parameters along GP15 (Figure 7 and Figure S2 in Supporting Information S1) are described in more detail and interpreted in terms of different physical and biogeochemical factors.

4.1. Lateral and Vertical Variations

First, we describe how our estimates of POC cycling rate parameters vary across different oceanic regions, and between the EZ and UMZ. Figure 8 and Table 2 show averages of posterior estimates in each of the four regions along GP15 in both the EZ and UMZ. We summarize the most salient points here. In the EZ, estimates of β_2' are lowest in the subarctic. Overall, β_2' increases from the EZ to the UMZ, but this trend is driven primarily by the low EZ values in the subarctic and subtropical South Pacific. The equatorial and subtropical North Pacific are characterized by high β_2' throughout the water column. Despite lowest estimates of β_2' in the EZ in the subarctic, this region has the largest estimates of β_2 in the EZ and UMZ due to the highest concentrations of P_S there. In all regions, our β_2 estimates are significantly greater (at the level of one standard error of the mean) in the EZ than in the UMZ due to the vertical attenuation of P_S. The subarctic region also has the largest estimates of β_{-2}, and as with β_2, estimates of β_{-2} for all regions are larger in the EZ than in the UMZ. While both β_{-2} and β_2 decrease from the EZ to the UMZ, the latter parameter decreases more strongly, resulting in an increase in β_{-2}/β_2 with depth in all regions. Although $\beta_{-1,S}$ generally attenuates with depth at all stations, it decreases more sharply within the EZ at the North and South Pacific subtropical gyre stations, resulting in more significant differences between the EZ and UMZ averages there than at the subarctic and equatorial stations, where surface estimates are more similar to those found at depth. Estimates of $\beta_{-1,L}$ are generally similar across regions and between the EZ and UMZ. The equatorial and North and South Pacific subtropical stations have similar estimates of w_S, whereas the w_S estimates are significantly smaller (at the level of one standard error) in the subarctic. Finally, estimates of w_L are significantly larger (at the level of one standard error) in the UMZ than in the EZ in all regimes.

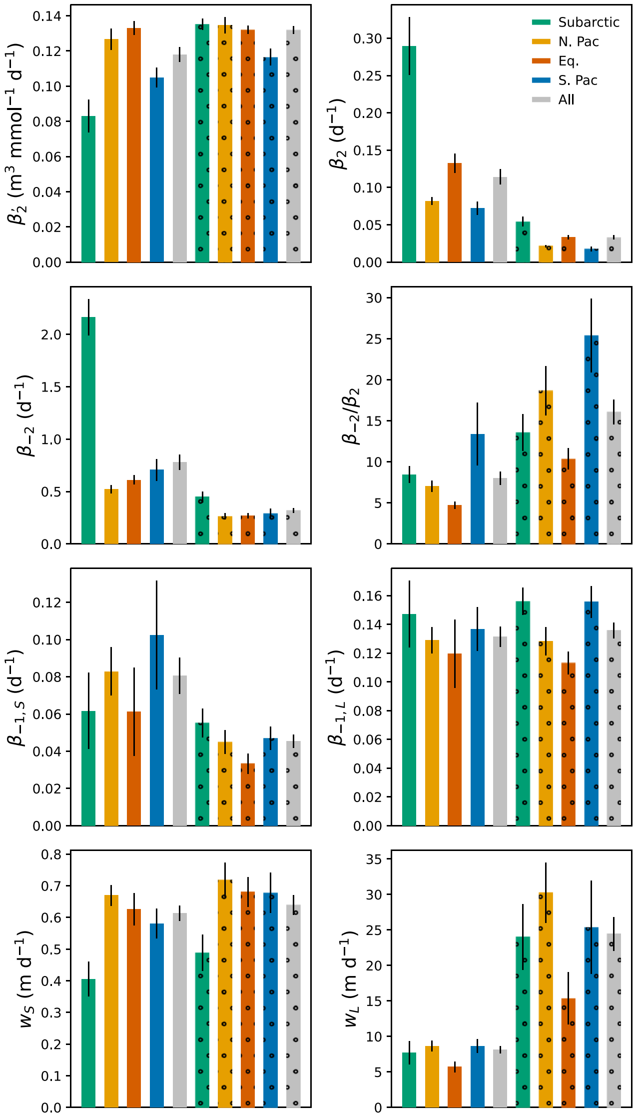

Figure 8. Averages of posterior estimates of the second- and first-order aggregation rate constants (β_2' and β_2, respectively), disaggregation rate constant (β_{-2}), ratio of disaggregation to aggregation rate constants (β_{-2}/β_2), remineralization rate constants for the SSF and LSF ($\beta_{-1,S}$ and $\beta_{-1,L}$, respectively), and settling speed of the SSF and LSF (w_S and w_L, respectively) grouped by oceanic region (colors) and depth interval (patterns). Plain bars correspond to the euphotic zone, while bars with circles correspond to the upper mesopelagic zone. Error bars indicate one standard error of the mean.

4.2. Settling Speeds

Differences in particle density and size might explain the increase in w_L with depth found in this study (Figures 7 and 8). Particle settling speed is often modeled using Stokes' Law: for a rigid spherical particle, the settling velocity increases with its excess density and the square of its diameter, and decreases with the viscosity of the surrounding fluid. Consider first the effect of particle density. Preferential remineralization of low-density labile organic matter near the surface (Nguyen et al., 2022) may contribute to the relatively large fraction of high-density biomineral and lithogenic material in deep particles (Xiang et al., 2022), thereby enhancing settling speed. Using sediment trap data from the Equatorial Pacific and Arabian Sea, Berelson (2002) inferred an increase in particle settling speed with depth and showed that this increase may have been due to a decrease in the fraction of organic carbon in particles. This result is consistent with a density-driven control of settling speed caused by preferential loss of low density material from remineralization of POC. Using lead and polonium isotopes, Villa-Alfageme et al. (2016) also inferred that particle settling speeds increased with depth at both oligotrophic and mesotrophic sites in the North Atlantic. In addition to remineralization, they pointed to aggregation in the UMZ as a possible driver for the downward increase in particle settling speed. Because estimates of particle density along GP15 are not currently available, we restrict our discussion to other possible explanations for the increase in particle sinking speed with depth which have been proposed in the literature. As estimates of particle density become available in the future, one may be able to relate variations in particle density to variations in particle sinking speed. Likewise, information about particle size distributions has not been gathered along GP15. A preliminary estimate of the distribution of particle mass between the two size fractions sampled by LVISF suggests an increased proportion of mass in the LSF with depth in the UMZ, which could be consistent with our inference of larger w_L at depth.

Next, consider the effect of seawater viscosity. We calculate dynamic viscosity from temperature and salinity (CTD data) at depths that are coincident with our settling speed estimates (Lam & Bishop, 2007). Particle settling speeds are expected to be greater in low latitudes than in high latitudes due to the relatively low viscosity of warm waters (Millero, 1974). Xiang et al. (2022) proposed that high seawater viscosity in the Arctic partly explained the low settling velocities there compared to those at subtropical locations. However, our results do not suggest an effect of seawater viscosity on particle settling speed in either the SSF or LSF, despite the change in dynamic viscosity by about a factor of two across the transect (Figure S3 in Supporting Information S1). In fact, the higher settling speeds in large particles tend to be found in waters with high viscosity, showing that the viscous drag on particles is not a primary control on settling speed. Indeed, several other studies have also found no relationship between seawater temperature and particle settling speed (Iversen & Ploug, 2013; McDonnell et al., 2015; Trull et al., 2008). Clearly, other factors such as differences in particle shape, density and size appeared to have been more important along GP15.

4.3. POC Settling Fluxes

Particle settling speed, along with POC concentration, at the base of the EZ controls the settling POC flux out of the EZ. Buesseler (1998) concluded that throughout much of the ocean, POC is efficiently recycled in the EZ such that only a low fraction (<5%–10%) is exported out of the sunlit layer. However, efficient recycling of organic material may not occur in highly productive regions, such as during phytoplankton blooms and in the Southern Ocean (Maiti et al., 2013). In these regions, a temporal lag between production and export may be

Table 2

Posterior Estimates of Non-Uniform Particulate Organic Carbon Cycling Parameters Averaged by Oceanic Region

Regime	β'_2 (m^3 $mmol^{-1}$ d^{-1})	β_2 (d^{-1})	β_{-2} (d^{-1})	β_{-2}/β_2 (unitless)	$\beta_{-1,S}$ (d^{-1})	$\beta_{-1,L}$ (d^{-1})	w_S (m d^{-1})	w_L (m d^{-1})
Subarc (10)	0.08 ± 0.01	0.29 ± 0.04	2.17 ± 0.17	8.44 ± 1.02	0.06 ± 0.02	0.15 ± 0.02	0.40 ± 0.05	7.69 ± 1.63
N Pac (43)	0.13 ± 0.01	0.08 ± 0.01	0.52 ± 0.04	7.03 ± 0.69	0.08 ± 0.01	0.13 ± 0.01	0.67 ± 0.03	8.64 ± 0.77
Eq (10)	0.13 ± 0.00	0.13 ± 0.01	0.61 ± 0.05	4.69 ± 0.44	0.06 ± 0.02	0.12 ± 0.02	0.63 ± 0.05	5.71 ± 0.76
S Pac (13)	0.10 ± 0.01	0.07 ± 0.01	0.71 ± 0.10	13.40 ± 3.83	0.10 ± 0.03	0.14 ± 0.02	0.58 ± 0.05	8.65 ± 0.98
All (76)	0.12 ± 0.00	0.11 ± 0.01	0.78 ± 0.07	8.00 ± 0.82	0.08 ± 0.01	0.13 ± 0.01	0.61 ± 0.02	8.13 ± 0.53
Subarc (17)	0.14 ± 0.00	0.05 ± 0.01	0.45 ± 0.05	13.55 ± 2.24	0.06 ± 0.01	0.16 ± 0.01	0.49 ± 0.06	24.03 ± 4.62
N Pac (22)	0.13 ± 0.00	0.02 ± 0.00	0.26 ± 0.03	18.67 ± 3.01	0.04 ± 0.01	0.13 ± 0.01	0.72 ± 0.06	30.27 ± 4.23
Eq (14)	0.13 ± 0.00	0.03 ± 0.00	0.27 ± 0.02	10.35 ± 1.30	0.03 ± 0.01	0.11 ± 0.01	0.68 ± 0.05	15.36 ± 3.68
S Pac (7)	0.12 ± 0.00	0.02 ± 0.00	0.29 ± 0.05	25.37 ± 4.48	0.05 ± 0.01	0.16 ± 0.01	0.68 ± 0.06	25.37 ± 6.58
All (60)	0.13 ± 0.00	0.03 ± 0.00	0.32 ± 0.02	16.06 ± 1.50	0.05 ± 0.00	0.14 ± 0.01	0.64 ± 0.03	24.45 ± 2.39

Note. Numbers in parentheses in the first column are the numbers of estimates considered to compute the means. Error shows one standard error of the mean. Parameters are averaged in subarctic (Subarc), North Pacific (N Pac), equatorial (Eq), and South Pacific (S Pac) regimes, as well as across the entire transect (All). The top five rows (regime name non-italicized) show values in the EZ, and the bottom five rows (regime name italicized) show values in the UMZ.

driven, for example, by the delayed response of zooplankton to an increase in the phytoplankton standing stock (Henson et al., 2015; Wassmann, 1998).

First, we examine how our estimates of the settling POC flux varies with trophic regime along GP15. Chl. a concentration averaged over the EZ is used as a convenient measure of the trophic regime at each station along GP15. Morel and Berthon (1989) used Chl. a concentration to classify trophic regimes into seven categories, *a*–*i*, where category *a* is the most oligotrophic and category *i* is the most eutrophic (note that Morel and Berthon based their classification from the sum of Chl. a and pheophytin, whilst we only consider Chl. a to assign a trophic status to each station; the difference is assumed inconsequential). Our stations fall roughly into categories *c*–*e*, and thus range from oligotrophic to mesotrophic. To test a possible relationship between trophic regime and export flux, our posterior estimates of total POC settling flux at the base of the EZ (the sum of $w_S P_S$ and $w_L P_L$) are regressed against Chl. a concentrations averaged over the EZ (Figure 9). We find a significant positive correlation between our estimates of settling POC flux and Chl. a concentration ($R^2 = 0.80$, $p < 0.05$, $N = 20$), with the highest fluxes in the subarctic gyre where Chl. a concentrations are highest and the lowest fluxes in the subtropical gyres where these concentrations are lowest.

Chl. a concentration alone may belie how different phytoplankton groups in the EZ influence POC production and export (Evans, 1988). Using a foodweb model and observations of POC flux from sediment traps, Boyd and Newton (1999) showed that subtle increases in the fraction of microplankton (diatoms and dinoflagellates) in the surface phytoplankton assemblage can result in large increases in POC flux at depth. This result was corroborated by particle imaging data and HPLC-based pigment analysis from the Atlantic, Pacific, and Indian Oceans as well as from the Mediterranean Sea: these data showed that POC fluxes out of the EZ are larger in regions where surface floral communities are dominated by microplankton, and are smaller in oligotrophic regions where picoplankton are the dominant group (Guidi et al., 2009). Guidi et al. (2009) argued that larger POC fluxes in microplankton-dominated regions result from (a) fast settling of aggregates packaged by physical coagulation or by zooplankton, and (b) a sizable fraction of particles escaping the EZ without being fragmented by zooplankton or degraded microbially. We also observe a significant positive correlation ($R^2 = 0.77$, $p < 0.05$, $N = 20$) between our estimates of the settling flux of total POC at the base of the EZ and the fraction of microplankton averaged over the EZ along GP15. Note that the relationship loses its significance when subarctic gyre stations are excluded (Figure 9), which may reflect the lack of microplankton in the rest of the transect.

Interestingly, while our results clearly show higher POC export at the mesotrophic (subarctic) stations where microplankton were more prevalent, the particle settling speeds at the base of the EZ at these stations are not considerably higher than those at oligotrophic (subtropical) stations (Figures 7 and 8). Instead, the higher EZ fluxes at mesotrophic stations were driven primarily by higher POC concentrations (Figure 2 and Figure S1 in Supporting Information S1). This pattern suggests that variations in POC flux along GP15 reflected differences

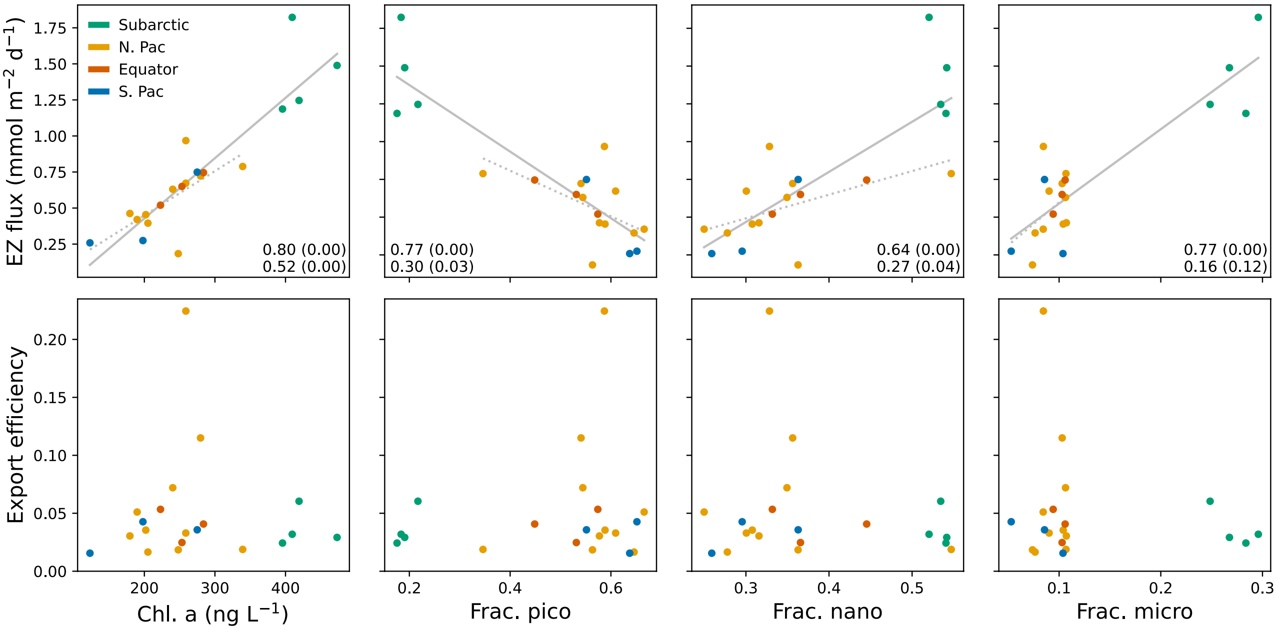

Figure 9. Estimates of particulate organic carbon (POC) export flux versus chlorophyll a (Chl. a) concentration and fractions of different size classes in the phytoplankton assemblage in the euphotic zone (EZ). Each marker represents an average for a single station. (Top) Settling flux of POC near the base of the EZ. In each panel, solid gray lines show the least squares fit to all data, while dashed gray lines show the least squares fit that exclude subarctic data (green circles). The top number in each panel corresponds to the fit shown by the solid line, while the bottom number corresponds to the fit shown by the dashed line. The number in front of parentheses is the squared correlation coefficient (R^2), and the number in parentheses is the p-value of the F-statistic. The sample size $N = 20$ for all regressions shown by the solid lines and $N = 16$ for all regressions shown by the dashed lines. (Bottom) Export efficiency, defined as the settling flux of total POC at the base of the EZ divided by the particle production rate integrated over the EZ.

in POC concentrations rather than in particle settling velocities, as recently inferred also for the North Atlantic, Eastern Tropical South Pacific, and Western Arctic Ocean (Xiang et al., 2022). Nevertheless, mesotrophic stations along GP15 were characterized by greater fractions of larger phytoplankton, which are coincident with higher POC concentrations and more export out of the EZ, while oligotrophic stations were characterized by greater fractions of smaller phytoplankton, which are coincident with lower POC concentrations and less export out of the EZ. Similarly, the total POC settling flux out of the EZ increases with the fraction of nanoplankton and decreases with the fraction of picoplankton in the floral assemblage (Figure 9).

If POC export is predominantly controlled by POC concentration rather than by particle settling speed, then we might expect that export efficiency (the fraction of POC produced photosynthetically in the EZ that is exported as settling POC at the base of the EZ) will remain constant even as the magnitude of export increases. Indeed, export efficiency throughout GP15 is relatively constant and low (generally <5%), with no enhancement in mesotrophic regions with higher abundance of microplankton (Figure 9). Such low export efficiencies fall on the lower range of model-based estimates in the world oceans (Siegel et al., 2023). They tend to occur in low productivity regions in the subtropics as well as in productive equatorial regions characterized by little seasonality (Henson et al., 2019), and are consistent with a tight relationship between production and export such that a high fraction of POC is recycled within the EZ (Buesseler, 1998). Speculatively, an export efficiency in the subarctic Pacific that is as low as that in oligotrophic gyres may reflect the fact that subarctic stations were sampled during non-bloom conditions.

Our inference of uniformly low export efficiency despite changes in trophic regime (cf., Morel & Berthon, 1989) and phytoplankton community composition (Figure 4) is surprising given accounts that high-export systems are dominated by microplankton (Boyd & Newton, 1999; Buesseler, 1998). Nevertheless, this result may be explained by the efficient recycling of POC in the upper water column in non-bloom conditions. For example, bacterial activity and zooplankton grazing may closely follow POC production during non-bloom conditions, such that organic carbon is rapidly extracted from the particulate pool (via remineralization and ingestion, respectively) in surface waters (Henson et al., 2019).

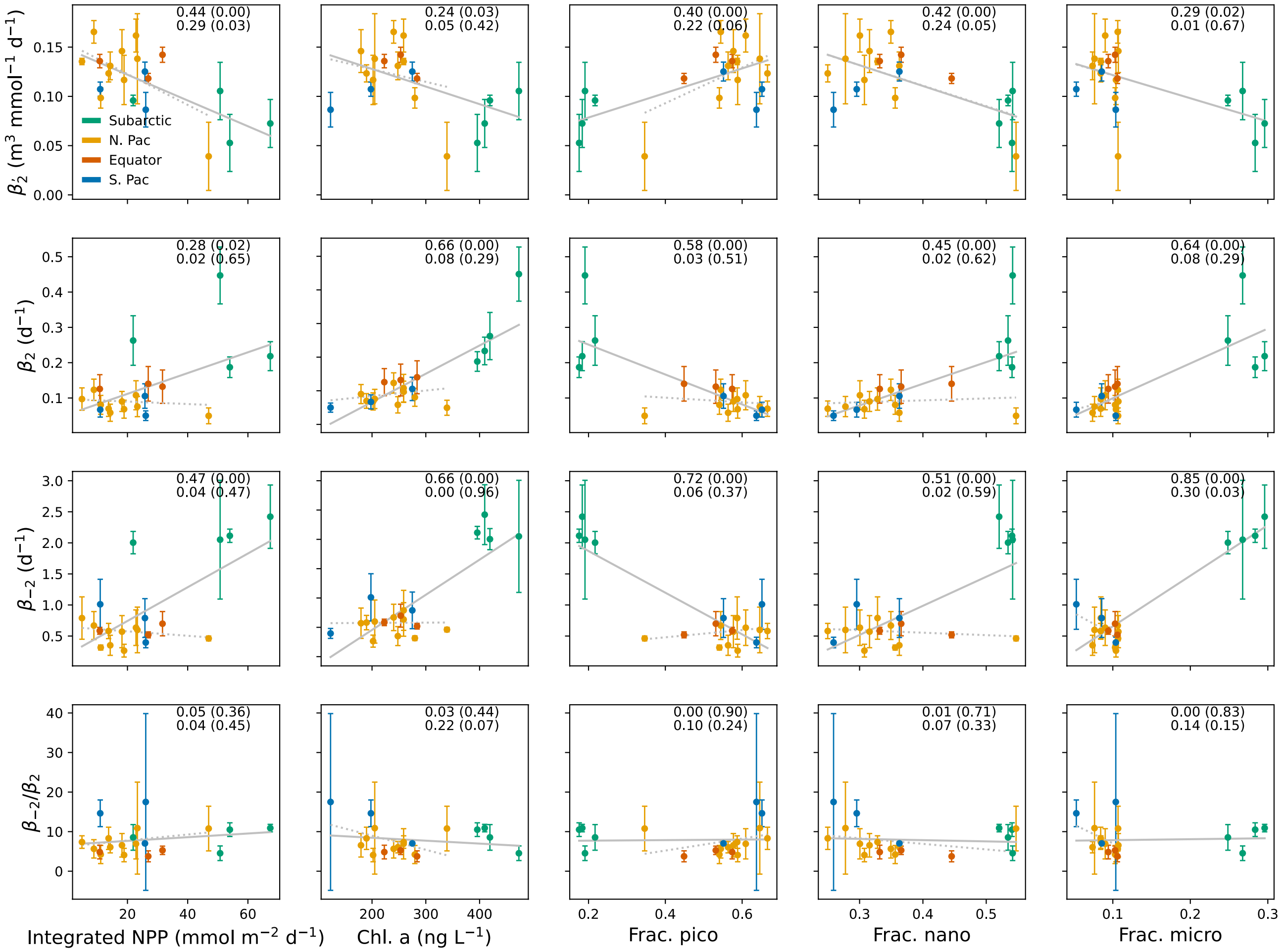

Figure 10. Posterior estimates of (dis)aggregation rate constants versus primary production integrated over the euphotic zone (EZ), EZ averages of chlorophyll a (Chl. a) concentration, and EZ averages of the fraction of different size classes in the phytoplankton assemblage. Error bars show one standard deviation. In each panel, solid gray line shows the least squares fit to all the data, while dashed gray line shows the least squares fit that excludes subarctic data (green circles). The top number in each panel corresponds to the fit shown by the solid line, while the bottom number corresponds to the fit shown by the dashed line. The number in front of parentheses is the squared correlation coefficient (R^2), and the number in parentheses is the p-value of the F-statistic. Sample size is $N = 20$ for all regressions shown by the solid lines and $N = 16$ for all regressions shown by the dashed lines.

4.4. Aggregation and Disaggregation

The composition of the phytoplankton community could also influence particle export via the ability of different phytoplankton groups to promote (dis)aggregation. In Figure 10, we regress the second- and first-order aggregation rate constants (β_2' and β_2 respectively), the disaggregation rate constant (β_{-2}), and the ratio β_{-2}/β_2, each averaged in the EZ, against our estimates of particle production rate integrated over the EZ, measurements of Chl. a averaged over the EZ, and fractions of pico-, nano-, and microplankton in the floral assemblage averaged over the EZ. For each regression, we either include (solid lines) or exclude (dashed lines) the subarctic estimates in order to test the sensitivity of the results to the inclusion/exclusion of these estimates.

The second-order aggregation rate constant, β_2', is intended to represent, at least partly, the cohesiveness of particles, as it removes the effect of particle concentration inherent in a first-order formulation (Jackson & Burd, 2015). Transparent exopolymer particles (TEPs) refer to gel-like material secreted by phytoplankton, and are thought to promote the formation of marine snow by facilitating the aggregation of smaller particles into larger units (Passow, 2002). Thus, more productive regions may be characterized by higher TEP concentrations and higher β_2' values. However, the correlations between our estimates of β_2' and particle production ($R^2 = 0.44$, $p < 0.05$, $N = 20$) and between our β_2' estimates and Chl. a concentration ($R^2 = 0.24$, $p < 0.05$, $N = 20$) in the EZ (Figure 10, top row), suggest negative relationships between particle stickiness and primary productivity or phytoplankton standing stock. On the other hand, we find a positive correlation between our estimates of β_2' and the fraction of picoplankton in the phytoplankton assemblage ($R^2 = 0.40$, $p < 0.05$, $N = 20$). High TEP concentrations have been observed in low-productivity waters (Wurl et al., 2011), and have been linked to the presence of *Prochlorococcus* (Iuculano et al., 2017) and *Synechococcus* (Zamanillo et al., 2019), two genera of picoplankton. We speculate from these results that higher TEP concentrations were present at the oligotrophic stations than at the mesotrophic stations along GP15.

The greater apparent stickiness of particles in picoplankton-dominated regions along GP15 suggests that aggregation may be more important in oligotrophic regions than previously thought. However, the greater particle concentrations of mesotrophic regions more than compensates for the reduced apparent cohesiveness of particles. The product of β_2' and P_S yields the first-order aggregation constant (β_2), which should consider the effects of both particle stickiness and particle concentration in the kinetics of aggregation. We find positive correlations, in the EZ, of β_2 with particle production ($R^2 = 0.28$, $p < 0.05$, $N = 20$) and Chl. a concentration ($R^2 = 0.66$, $p < 0.05$, $N = 20$) (Figure 10, second row). In the EZ, we also see a negative correlation of β_2 with the picoplankton fraction ($R^2 = 0.58$, $p < 0.05$, $N = 20$) and positive correlations with nanoplankton ($R^2 = 0.45$, $p < 0.05$, $N = 20$) and microplankton ($R^2 = 0.64$, $p < 0.05$, $N = 20$) fractions. Both results are likely due to larger P_S concentrations at more productive stations dominated by larger phytoplankton (Figure 4). They suggest that the effect of particle concentration overwhelms the influence of particle stickiness in the formation of aggregates.

The negative relationships of β_2' with the nanoplankton fraction ($R^2 = 0.42$, $p < 0.05$) and with the microplankton fraction ($R^2 = 0.29$, $p < 0.05$, $N = 20$) suggest that particles in more productive regions dominated by larger phytoplankton cells may be less cohesive, and as a result, more prone to disaggregation. Indeed, we observe positive correlations of the disaggregation rate constant (β_{-2}) with particle production ($R^2 = 0.47$, $p < 0.05$, $N = 20$), Chl. a concentration ($R^2 = 0.66$, $p < 0.05$, $N = 20$), and fractions of nanoplankton ($R^2 = 0.51$, $p < 0.05$, $N = 20$) and microplankton ($R^2 = 0.85$, $p < 0.05$, $N = 20$) in the EZ (Figure 10, third row).

Laboratory (Dilling & Alldredge, 2000; Goldthwait et al., 2004; Lampitt et al., 1990) and modeling (T. R. Anderson & Tang, 2010) experiments have shown that zooplankton may fragment particles during grazing and swimming. Zooplankton may also be partially responsible for the general decrease in depth in our β_{-2} estimates throughout GP15 (Figure 7). Using backscatter data from ARGO floats, Briggs et al. (2020) inferred a decrease in particle fragmentation rate with depth in the North Atlantic and Southern Ocean, which they attributed to zooplankton grazing preferentially closer to the sea surface and to the break-up of more fragile aggregates at shallower depths. The influence of zooplankton activity on particle fragmentation is difficult to measure, and as far as we know, it has not been directly tested in the field. Here, we use our estimates of zooplankton ingestion rate (β_3) as a metric for assessing zooplankton activity in the EZ. We do not see a significant correlation between our estimates of β_{-2} in the EZ and of the zooplankton ingestion rate (β_3) along GP15 ($R^2 = 0.16$, $p > 0.05$, $N = 20$; not shown), but emphasize that in addition to not being well constrained, β_3 may not be a robust metric for assessing zooplankton fragmenting activity. Hence, we cannot support nor refute the hypothesis of zooplankton-mediated fragmentation. In addition to biological processes, physical processes may also promote the break-up of marine aggregates (Burd & Jackson, 2009). A physical process of particle disaggregation is fragmentation by fluid shear (Burd & Jackson, 2009), but we are not able to constrain this process with the available data for GP15.

Lastly, we find no significant relationship between the rate constant ratio β_{-2}/β_2 and particle production or Chl. a concentration in the EZ (Figure 10, bottom row), which are both indicative of trophic regime. Both the first order aggregation rate constant and the first order disaggregation rate constant increase with trophic regime, such that their ratio remains relatively constant (Figure 10). Both in the EZ and UMZ, β_{-2}/β_2 always exceeds 1, showing that the kinetics of particle disaggregation are faster than those of particle aggregation along GP15. A relatively high rate constant of particle break-up compared to particle aggregation has been inferred in previous studies from Th isotope and particle concentration data (Clegg & Whitfield, 1990; Murnane, 1994). Furthermore, β_{-2}/β_2 tends to increase with depth from the EZ to the UMZ throughout GP15 (Figure 8): while β_2 and β_{-2} both decrease with depth, the former rate constant decreases faster than the latter, leading to higher β_{-2}/β_2 ratios in deep waters.

4.5. Remineralization

Another parameter that is expected to exhibit variations throughout the transect is the remineralization rate constant. Particles are colonized by microbes in surface waters; both microbial diversity and abundance decrease as the particles sink (Iversen, 2023). While particles in surface waters are richer in organic substrates that can support fast growing microbes and promote remineralization, nutrient-poor particles at depth are inhabited by microbes with slower growth cycles (Nguyen et al., 2022). In addition to the lability of particulate organic matter, vertical variations in the remineralization rate constant may reflect differences in temperature, as warm surface waters are expected to support faster microbial growth rates than cold deep waters (Cram et al., 2018; Laufkötter et al., 2017).

Our estimates of the remineralization rate constant for the small size fraction ($\beta_{-1,S}$) along GP15 generally decrease with depth (Figures 7 and 8). A decrease in the remineralization rate constant with depth has been inferred in previous model studies (Clegg et al., 1991), and is consistent with an influence of temperature on microbial activity. Indeed, higher remineralization rates in warmer waters have been reported both in the field (Marsay et al., 2015) and in model studies (Cram et al., 2018; Laufkötter et al., 2017). However, temperature did not seem to exert a clear influence on $\beta_{-1,S}$ and $\beta_{-1,L}$ along GP15 (Figure S4 in Supporting Information S1), suggesting that the decrease in microbial abundance on particles (Iversen, 2023) and the decrease in remineralization rate constant with depth were not due to temperature, but rather to other factors, such as a decrease in particle lability (Nguyen et al., 2022).

In addition to particle lability and seawater temperature, the concentration of dissolved O_2 may also influence the remineralization of POC (Gong et al., 2016). However, as for temperature, we do not see evidence for an effect of dissolved O_2 concentration on $\beta_{-1,S}$ and $\beta_{-1,L}$ (Figure S4 in Supporting Information S1). Two modeling studies (Cram et al., 2018; Laufkötter et al., 2017) found that the attenuation of POC flux from remineralization had a dependency on O_2 concentration that was generally only important in oxygen minimum zones, particularly where O_2 concentrations approached the 5–30 μM range of half saturation constants for metabolic activity. The GP15 transect frequently sampled waters <30 μM in the subarctic and subtropical North Pacific and Equatorial Pacific (Figure 5). It is thus surprising that our results show no indication that the remineralization rate constant was lower where dissolved O_2 was less than 30 μM (Figure S4 in Supporting Information S1). Other studies have shown that the remineralization length scale for POC flux does appear to increase through truly oxygen deficient zones (e.g., Pavia et al., 2019). We thus suggest that the apparent half saturation constant for O_2 is lower than 5–30 μM along GP15 and that the remineralization rate constant may only be affected in truly oxygen deficient waters, where dissolved O_2 is undetectable.

Finally, note that in the EZ, our posterior estimates of the rate constants for remineralization of POC in the SSF ($\beta_{-1,S}$) and for particle aggregation (β_2), both of which remove POC from the small size fraction, are of the same order of magnitude as the zooplankton ingestion rate constant (β_3; see Figures 6 and 8). This result underscores the necessity of considering zooplankton grazing when modeling the cycling of POC in the upper water column (see also Amaral et al., 2022), which has often been neglected in previous studies.

5. Summary and Perspectives

In this study, we use an inverse method to constrain particle cycling processes from size-fractionated POC concentration data, which were collected in the upper 600 m along the GEOTRACES Pacific meridional transect GP15 from September to November of 2018. We derive, from the size-fractionated data and other observations along GP15, estimates of the rates of particle production, settling, aggregation, disaggregation, remineralization, and vertical transport due to migrating zooplankton at different depths in different oceanic environments. The inverse method considers prior estimates and their uncertainties in the estimation of rate parameters along GP15. A Monte Carlo approach is used to produce data inversions for a wide range of prior estimates. To our knowledge, this is the first study that estimates depth-varying particle cycling rate constants over a broad transect crossing different ocean biogeochemical regimes. We find coherent horizontal and vertical variations in several particle cycling rate constants, which are summarized below.

While our estimates of settling speed in the small size fraction (w_S) range between 0.2 and 1 m d^{-1} and do not vary much with depth at a given station, our estimates of settling speed in the large size fraction (w_L) tend to increase with depth below the EZ, with a maximum speed of roughly 66 m d^{-1} at one station. The downward increase in w_L may be due to an increase in particle density with depth, as relatively light and labile particulate material is preferentially remineralized closer to the surface. No dependence of particle settling speed on seawater viscosity is found.

According to our analysis, the highest settling fluxes of POC out of the EZ occurred in the subarctic gyre, while the lowest fluxes occurred in the subtropical gyres. The magnitude of the POC export flux varies with latitude, largely as a result of variations in POC concentration rather than in particle settling speed. The relatively low (<5%) and uniform export efficiency along GP15 which is revealed by our analysis suggests that POC in the EZ was rapidly recycled through, for example, zooplankton ingestion and microbially mediated remineralization at the time of sampling (boreal autumn and austral spring).

We find a negative relationship between the particle cohesiveness, as approximated by the second-order aggregation rate constant (β_2'), and indices of trophic regime, suggesting that particles in low productivity regions dominated by picoplankton are more likely to coalesce after colliding. On the other hand, particles in mesotrophic waters with higher fractions of microplankton may be less cohesive and more prone to fragmentation, as indicated by a positive relationship between the disaggregation rate constant (β_{-2}) and indices of trophic regime. However, higher POC concentrations in more productive regions appear to compensate for lower particle stickiness there, resulting in a relatively uniform ratio $\beta_{-2}/\left(\beta_2' P_S\right) = \beta_{-2}/\beta_2$.

Finally, we found that the remineralization rate constant for POC in the small size fraction was highest in surface waters and decreased with depth, which is consistent with greater microbial colonization and remineralization of particles near the surface. We do not find a dependence of the remineralization rate constant (in either size fraction) on temperature or dissolved O_2 concentration. We also find that the rate constants for the remineralization of POC in the SSF ($\beta_{-1,S}$) and for particle aggregation (β_2) along GP15 in the EZ were of the same order of magnitude as the rate constant for zooplankton ingestion of POC. This result emphasizes the importance of zooplankton in influencing the distribution of POC in the upper water column.

The main limitations of this work are clarified in order to identify possible lines of future research. First, we use a one-dimensional steady state model that neglects temporal variability and lateral transport processes, as well as vertical transport by advection and mixing. In our analysis of GP15 data, the model equations are required to be perfectly satisfied, which implies that our inverse estimates are not free of potential biases. Second, the segmentation of the particle population into two size classes, albeit motivated by the nature of in-situ sampling, is a poor representation of the size spectrum of marine particles. There is inherent ambiguity in the interpretation of parameters of models which are characterized by a reduced number of particle size classes. Third, we assume that primary production is a source of POC only in the small size fraction. This choice is motivated by an expectation that most algal particles will indeed be produced in the small size fraction, though we acknowledge that some phytoplankton groups, for example, certain diatom species, produce cells that are larger than 51 μm (Takahashi, 1986). Thus, the model may drive aggregation or zooplankton egestion (sources of large POC) to be artificially high in regions where microplankton are more prevalent. Finally, error (co)variances for the prior estimates are difficult to constrain, which is an additional source of uncertainty in the interpretation of the transect data. While this study is limited to a description of lateral and vertical variations in particle cycling rate constants and POC settling fluxes out of the EZ, future efforts should explore the relative importance of different particle cycling processes in downward POC export (e.g., comparing the magnitude of inputs of POC into the UMZ by zooplankton DVM and gravitational settling).

Despite these limitations, our analysis of GP15 data yields insight into the cycling of POC in the upper water column in the North and South Pacific. Consistent lateral and vertical gradients in a number of particle cycling rate parameters are inferred, and some of these gradients could be interpreted in biogeochemical terms. Perhaps our most tangible result is the inference of uniformly low (<5%) export efficiency across the transect, suggesting that particulate organic matter was rapidly recycled in the EZ, even in mesostrophic systems. Moreover, our model represents POC cycling with greater detail than global ocean biogeochemical models, which often omit vertical variations in rate parameters as well as the effects of migrating zooplankton.

Global warming is expected to lead to significant changes in a number of ocean properties, including an increase in ocean temperature, a decrease in nutrient supply to the EZ, a decrease in dissolved O_2 concentrations, and shifts in phytoplankton populations (Kwiatkowski et al., 2020). Model experiments have suggested that these changes may result, for example, in a reduction in POC export to depth (Yamamoto et al., 2018) and in increased bacterial respiration (Kim et al., 2023). According to our data-based results, it is unclear whether warming, deoxygenation, and changes in phytoplankton community composition will noticeably modify the rates at which POC is cycled in the EZ and UMZ of the Pacific Ocean. We did, however, find that POC export to depth is closely tied to the magnitude of primary production, which emphasizes the need to understand the various controls on primary production in order to predict the response of the biological pump to external perturbations.

Data Availability Statement

The code and input data used to generate the results within this paper are archived at https://zenodo.org/records/10223612 (Amaral, 2023). Original data sources are also described here where appropriate. Diffuse attenuation coefficient (K_d) data used for obtaining prior estimates of the vertical scale for particle production (L_P) were produced by the NASA Ocean Biology Processing Group (2018) and were downloaded with the Giovanni online data system, developed and maintained by the NASA GES DISC (Acker & Leptoukh, 2007). These data were downloaded from Giovanni as an Animation plot of the MODISA_L3m_KD_8d_4k_v2018 variable with a date range from 22 September 2018 to 24 November 2018 and a bounding geographic box of (−157, −20, −151, 57). Downloads from Giovanni require user registration. Estimates of net primary productivity from the Carbon-based Production Model (Westberry et al., 2008, http://sites.science.oregonstate.edu/ocean.productivity/) are used to calculate prior estimates of particle production rate at the surface ($\dot{P}_{S,0}$). These estimates were downloaded from the 2160 by 4320 8-day HDF files from MODIS r2018 (GSM) data from 22 September 2018 to 24 November 2018 (year days 265–328; updated 5 March 2018). All data collected from the R.V. Roger Revelle during the GP15 cruise can be downloaded from BCO-DMO (https://www.bco-dmo.org/project/695926). These include temperature and O_2 data measured from CTD sensors (Casciotti et al., 2019; Cutter et al., 2019), nutrient data (Casciotti et al., 2021a, 2021b), pigment data (Cutter et al., 2023a, 2023b), and estimates of vertical POC flux from ^{234}Th (Buesseler, 2021a, 2021b).

Acknowledgments
This study was supported by NSF-OCE 1736601 to PJL and NSF-OCE 1829790 to OM. VJA was supported by the NSF Graduate Research Fellowship Program and the UC Eugene Cota-Robles Fellowship. We would like to thank the crew of the R.V. Roger Revelle during the 2018 GEOTRACES GP15 cruise for conducting ship operations. We are especially grateful for the efforts contributed by the "pump team" in collecting samples (Steve Pike, Emilie Le Roy, Paul Henderson, Yang Xiang, and Virginie Sanial). We thank Nicola Paul, Alyson Santoro, Matthieu Bressac, and Philip Boyd for contributing data to help constrain prior estimates of particle remineralization rate. We also acknowledge the MODIS mission scientists and associated NASA personnel for the production of the satellite data used in this work. Finally, we thank the two anonymous reviewers whose comments helped guide the revision of this manuscript.

References

Acker, J. G., & Leptoukh, G. (2007). Online analysis enhances use of NASA Earth science data. *Eos, Transactions American Geophysical Union*, *88*(2), 14–17. https://doi.org/10.1029/2007EO020003

Amaral, V. J. (2023). amaralvin7/pyrite: GBC submission [Software]. Zenodo. https://doi.org/10.5281/zenodo.10223612

Amaral, V. J., Lam, P. J., Marchal, O., Roca-Martí, M., Fox, J., & Nelson, N. B. (2022). Particle cycling rates at Station P as estimated from the inversion of POC concentration data. *Elementa: Science of the Anthropocene*, *10*(1), 00018. https://doi.org/10.1525/elementa.2021.00018

Anderson, R. F., Cheng, H., Edwards, R. L., Fleisher, M. Q., Hayes, C. T., Huang, K.-F., et al. (2016). How well can we quantify dust deposition to the ocean? *Philosophical Transactions of the Royal Society A: Mathematical, Physical & Engineering Sciences*, *374*(2081), 20150285. https://doi.org/10.1098/rsta.2015.0285

Anderson, T. R., & Tang, K. W. (2010). Carbon cycling and POC turnover in the mesopelagic zone of the ocean: Insights from a simple model. *Deep Sea Research Part II: Topical Studies in Oceanography*, *57*(16), 1581–1592. https://doi.org/10.1016/j.dsr2.2010.02.024

Berelson, W. M. (2002). Particle settling rates increase with depth in the ocean. *Deep Sea Research Part II: Topical Studies in Oceanography*, *49*(1–3), 237–251. https://doi.org/10.1016/S0967-0645(01)00102-3

Bishop, J. K. B., Amaral, V. J., Lam, P. J., Wood, T. J., Lee, J.-M., Laubach, A., et al. (2022). Transmitted cross-polarized light detection of particulate inorganic carbon concentrations and fluxes in the ocean water column: Ships to ARGO floats. *Frontiers in Remote Sensing*, *3*, 837938. https://doi.org/10.3389/frsen.2022.837938

Boyd, P. W., & Newton, P. (1999). Does planktonic community structure determine downward particulate organic carbon flux in different oceanic provinces? *Deep Sea Research Part I: Oceanographic Research Papers*, *46*(1), 63–91. https://doi.org/10.1016/S0967-0637(98)00066-1

Briggs, N., Dall'Olmo, G., & Claustre, H. (2020). Major role of particle fragmentation in regulating biological sequestration of CO_2 by the oceans. *Science*, *367*(6479), 791–793. https://doi.org/10.1126/science.aay1790

Buesseler, K. O. (1998). The decoupling of production and particulate export in the surface ocean. *Global Biogeochemical Cycles*, *12*(2), 297–310. https://doi.org/10.1029/97GB03366

Buesseler, K. O. (2021a). Water column total and particulate Thorium-234 from Leg 1 (Seattle, WA to Hilo, HI) of the US GEOTRACES Pacific Meridional Transect (PMT) cruise (GP15, RR1814) on R/V Roger Revelle from September to October 2018. (Version 2) [Dataset]. Biological and Chemical Oceanography Data Management Office (BCO-DMO). https://doi.org/10.26008/1912/bco-dmo.777951.6

Buesseler, K. O. (2021b). Water column total and particulate Thorium-234 from Leg 2 (Hilo, HI to Papeete, French Polynesia) of the US GEOTRACES Pacific Meridional Transect (PMT) cruise (GP15, RR1815) on R/V Roger Revelle from October to November 2018. (Version 2) [Dataset]. Biological and Chemical Oceanography Data Management Office (BCO-DMO). https://doi.org/10.26008/1912/bco-dmo.777951.6

Burd, A. B. (2013). Modeling particle aggregation using size class and size spectrum approaches: Modeling particle aggregation. *Journal of Geophysical Research: Oceans*, *118*(7), 3431–3443. https://doi.org/10.1002/jgrc.20255

Burd, A. B., & Jackson, G. A. (2009). Particle aggregation. *Annual Review of Marine Science*, *1*(1), 65–90. https://doi.org/10.1146/annurev.marine.010908.163904

Calbet, A. (2001). Mesozooplankton grazing effect on primary production: A global comparative analysis in marine ecosystems. *Limnology and Oceanography*, *46*(7), 1824–1830. https://doi.org/10.4319/lo.2001.46.7.1824

Casciotti, K. L., Cutter, G. A., & Lam, P. J. (2019). CTD profiles from the ODF rosette on the US GEOTRACES Pacific Meridional Transect (PMT) cruise (GP15) from September to November 2018. (Version 0) [Dataset]. Biological and Chemical Oceanography Data Management Office (BCO-DMO). https://doi.org/10.26008/1912/bco-dmo.778168.2

Casciotti, K. L., Cutter, G. A., & Lam, P. J. (2021a). Bottle file from Leg 1 (Seattle, WA to Hilo, HI) of the US GEOTRACES Pacific Meridional Transect (PMT) cruise (GP15, RR1814) on R/V Roger Revelle from September to October 2018. (Version 6) [Dataset]. Biological and Chemical Oceanography Data Management Office (BCO-DMO). https://doi.org/10.26008/1912/bco-dmo.777951.6

Casciotti, K. L., Cutter, G. A., & Lam, P. J. (2021b). Bottle file from Leg 2 (Hilo, HI to Papeete, French Polynesia) of the US GEOTRACES Pacific Meridional Transect (PMT) cruise (GP15, RR1815) on R/V Roger Revelle from October to November 2018. (Version 5) [Dataset]. Biological and Chemical Oceanography Data Management Office (BCO-DMO). https://doi.org/10.26008/1912/bco-dmo.824867.5

Clegg, S. L., Bacon, M. P., & Whitfield, M. (1991). Application of a generalized scavenging model to thorium isotope and particle data at equatorial and high-latitude sites in the Pacific Ocean. *Journal of Geophysical Research*, *96*(C11), 20655–20670. https://doi.org/10.1029/91JC01784

Clegg, S. L., & Whitfield, M. (1990). A generalized model for the scavenging of trace metals in the open ocean–II. Thorium scavenging. *Deep Sea Research*, *38*(1), 91–120. https://doi.org/10.1016/0198-0149(91)90056-L

Cram, J. A., Weber, T., Leung, S. W., McDonnell, A. M. P., Liang, J., & Deutsch, C. (2018). The role of particle size, ballast, temperature, and oxygen in the sinking flux to the deep sea. *Global Biogeochemical Cycles*, *32*(5), 858–876. https://doi.org/10.1029/2017GB005710

Cutter, G. A., Casciotti, K. L., & Lam, P. J. (2019). CTD data from the GTC rosette on the US GEOTRACES Pacific Meridional Transect (PMT) cruise (GP15) from September to November 2018. (Version 0) [Dataset]. Biological and Chemical Oceanography Data Management Office (BCO-DMO). https://doi.org/10.26008/1912/bco-dmo.778332.2

Cutter, G. A., Casciotti, K. L., & Lam, P. J. (2023a). Pigment concentrations determined by HPLC from samples collected on Leg 1 (Seattle, WA to Hilo, HI) of the US GEOTRACES Pacific Meridional Transect (PMT) cruise (GP15, RR1814) on R/V Roger Revelle from September to October 2018. (Version 1) [Dataset]. Biological and Chemical Oceanography Data Management Office (BCO-DMO). https://doi.org/10.26008/1912/bco-dmo.914655.1

Cutter, G. A., Casciotti, K. L., & Lam, P. J. (2023b). Pigment concentrations determined by HPLC from samples collected on Leg 2 (Hilo, HI to Papeete, French Polynesia) of the US GEOTRACES Pacific Meridional Transect (PMT) cruise (GP15, RR1815) on R/V Roger Revelle from October to November 2018. (Version 1) [Dataset]. Biological and Chemical Oceanography Data Management Office (BCO-DMO). https://doi.org/10.26008/1912/bco-dmo.914845.1

Dilling, L., & Alldredge, A. L. (2000). Fragmentation of marine snow by swimming macrozooplankton: A new process impacting carbon cycling in the sea. *Deep Sea Research Part I: Oceanographic Research Papers*, *47*(7), 1227–1245. https://doi.org/10.1016/S0967-0637(99)00105-3

Ducklow, H., Steinberg, D., & Buesseler, K. (2001). Upper ocean carbon export and the biological pump. *Oceanography*, *14*(4), 50–58. https://doi.org/10.5670/oceanog.2001.06

Evans, G. T. (1988). A framework for discussing seasonal succession and coexistence of phytoplankton species: Phytoplankton species succession. *Limnology and Oceanography*, *33*(5), 1027–1036. https://doi.org/10.4319/lo.1988.33.5.1027

Gdaniec, S., Roy-Barman, M., Levier, M., Valk, O., van der Loeff, M. R., Foliot, L., et al. (2020). ^{231}Pa and ^{230}Th in the Arctic Ocean: Implications for boundary scavenging and ^{231}Pa–^{230}Th fractionation in the Eurasian Basin. *Chemical Geology*, *532*, 119380. https://doi.org/10.1016/j.chemgeo.2019.119380

Goldthwait, S., Yen, J., Brown, J., & Alldredge, A. (2004). Quantification of marine snow fragmentation by swimming euphausiids. *Limnology and Oceanography*, *49*(4), 940–952. https://doi.org/10.4319/lo.2004.49.4.0940

Gong, X., Garcia-Robledo, E., Schramm, A., & Revsbech, N. P. (2016). Respiratory kinetics of marine bacteria exposed to decreasing oxygen concentrations. *Applied and Environmental Microbiology*, *82*(5), 1412–1422. https://doi.org/10.1128/AEM.03669-15

Guidi, L., Stemmann, L., Jackson, G. A., Ibanez, F., Claustre, H., Legendre, L., et al. (2009). Effects of phytoplankton community on production, size, and export of large aggregates: A world-ocean analysis. *Limnology and Oceanography*, *54*(6), 1951–1963. https://doi.org/10.4319/lo.2009.54.6.1951

Henson, S., Le Moigne, F., & Giering, S. (2019). Drivers of carbon export efficiency in the global ocean. *Global Biogeochemical Cycles*, *33*(7), 891–903. https://doi.org/10.1029/2018GB006158

Henson, S., Yool, A., & Sanders, R. (2015). Variability in efficiency of particulate organic carbon export: A model study. *Global Biogeochemical Cycles*, *29*(1), 33–45. https://doi.org/10.1002/2014GB004965

Iuculano, F., Mazuecos, I. P., Reche, I., & Agustí, S. (2017). Prochlorococcus as a possible source for transparent exopolymer particles (TEP). *Frontiers in Microbiology*, *8*, 709. https://doi.org/10.3389/fmicb.2017.00709

Iversen, M. H. (2023). Carbon export in the ocean: A biologist's perspective. *Annual Review of Marine Science*, *15*(1), 357–381. https://doi.org/10.1146/annurev-marine-032122-035153

Iversen, M. H., & Ploug, H. (2013). Temperature effects on carbon-specific respiration rate and sinking velocity of diatom aggregates – Potential implications for deep ocean export processes. *Biogeosciences*, *10*(6), 4073–4085. https://doi.org/10.5194/bg-10-4073-2013

Jackson, G. A., & Burd, A. B. (2015). Simulating aggregate dynamics in ocean biogeochemical models. *Progress in Oceanography*, *133*, 55–65. https://doi.org/10.1016/j.pocean.2014.08.014

Kenyon, J. A. (2022). *Anthropogenic and natural radioisotopes as tracers for contaminant sources and particulate fluxes* (Doctoral thesis). Massachusetts Institute of Technology and Woods Hole Oceanographic Institution. Woods Hole Open Access Server. https://doi.org/10.1575/1912/27995

Kim, H. H., Laufkötter, C., Lovato, T., Doney, S. C., & Ducklow, H. W. (2023). Projected 21st-century changes in marine heterotrophic bacteria under climate change. *Frontiers in Microbiology*, *14*, 1049579. https://doi.org/10.3389/fmicb.2023.1049579

Krishnaswami, S., Lal, D., Somayajulu, B. L. K., Weiss, R. F., & Craig, H. (1976). Large-volume in-situ filtration of deep Pacific waters: Mineralogical and radioisotope studies. *Earth and Planetary Science Letters*, *32*(2), 420–429. https://doi.org/10.1016/0012-821X(76)90082-0

Krishnaswami, S., Sarin, M., & Somayajulu, B. (1981). Chemical and radiochemical investigations of surface and deep particles of the Indian Ocean. *Earth and Planetary Science Letters*, *54*(1), 81–96. https://doi.org/10.1016/0012-821X(81)90071-6

Kwiatkowski, L., Torres, O., Bopp, L., Aumont, O., Chamberlain, M., Christian, J. R., et al. (2020). Twenty-first century ocean warming, acidification, deoxygenation, and upper-ocean nutrient and primary production decline from CMIP6 model projections. *Biogeosciences*, *17*(13), 3439–3470. https://doi.org/10.5194/bg-17-3439-2020

Lam, P. J., & Bishop, J. K. (2007). High biomass, low export regimes in the Southern Ocean. *Deep Sea Research Part II: Topical Studies in Oceanography*, *54*(5–7), 601–638. https://doi.org/10.1016/j.dsr2.2007.01.013

Lam, P. J., Lee, J.-M., Heller, M. I., Mehic, S., Xiang, Y., & Bates, N. R. (2018). Size-fractionated distributions of suspended particle concentration and major phase composition from the U.S. GEOTRACES Eastern Pacific Zonal Transect (GP16). *Marine Chemistry*, *201*, 90–107. https://doi.org/10.1016/j.marchem.2017.08.013

Lam, P. J., Ohnemus, D. C., & Auro, M. E. (2015). Size-fractionated major particle composition and concentrations from the US GEOTRACES North Atlantic Zonal Transect. *Deep Sea Research Part II: Topical Studies in Oceanography*, *116*, 303–320. https://doi.org/10.1016/j.dsr2.2014.11.020

Lampitt, R. S., Noji, T., & Von Bodungen, B. (1990). What happens to zooplankton faecal pellets? Implications for material flux. *Marine Biology*, *104*(1), 15–23. https://doi.org/10.1007/BF01313152

Latasa, M., Bidigare, R. R., Ondrusek, M. E., & Kennicutt, M. C. (1996). HPLC analysis of algal pigments: A comparison exercise among laboratories and recommendations for improved analytical performance. *Marine Chemistry*, *51*(4), 315–324. https://doi.org/10.1016/0304-4203(95)00056-9

Laufkötter, C., John, J. G., Stock, C. A., & Dunne, J. P. (2017). Temperature and oxygen dependence of the remineralization of organic matter: Remineralization of organic matter. *Global Biogeochemical Cycles*, *31*(7), 1038–1050. https://doi.org/10.1002/2017GB005643

Lawrence, R. M., Shrikumar, A., Le Roy, E., Swift, J. H., Lam, P. J., Cutter, G., & Casciotti, K. L. (2022). Water mass analysis of the 2018 US GEOTRACES Pacific Meridional Transect (GP15). *ESS Open Archive*. https://doi.org/10.1002/essoar.10510438.1

Lerner, P., Marchal, O., Lam, P. J., Buesseler, K., & Charette, M. (2017). Kinetics of thorium and particle cycling along the U.S. GEOTRACES North Atlantic Transect. *Deep Sea Research Part I: Oceanographic Research Papers*, *125*, 106–128. https://doi.org/10.1016/j.dsr.2017.05.003

Maiti, K., Charette, M. A., Buesseler, K. O., & Kahru, M. (2013). An inverse relationship between production and export efficiency in the Southern Ocean. *Geophysical Research Letters*, *40*(8), 1557–1561. https://doi.org/10.1002/grl.50219

Marsay, C. M., Sanders, R. J., Henson, S. A., Pabortsava, K., Achterberg, E. P., & Lampitt, R. S. (2015). Attenuation of sinking particulate organic carbon flux through the mesopelagic ocean. *Proceedings of the National Academy of Sciences*, *112*(4), 1089–1094. https://doi.org/10.1073/pnas.1415311112

McDonnell, A. M. P., Boyd, P. W., & Buesseler, K. O. (2015). Effects of sinking velocities and microbial respiration rates on the attenuation of particulate carbon fluxes through the mesopelagic zone. *Global Biogeochemical Cycles*, *29*(2), 175–193. https://doi.org/10.1002/2014GB004935

McDonnell, A. M. P., & Buesseler, K. O. (2010). Variability in the average sinking velocity of marine particles. *Limnology and Oceanography*, *55*(5), 2085–2096. https://doi.org/10.4319/lo.2010.55.5.2085

McDonnell, A. M. P., & Buesseler, K. O. (2012). A new method for the estimation of sinking particle fluxes from measurements of the particle size distribution, average sinking velocity, and carbon content. *Limnology and Oceanography: Methods*, *10*(5), 329–346. https://doi.org/10.4319/lom.2012.10.329

Millero, F. J. (1974). Seawater as a multicomponent electrolyte solution. In *The Sea*. In *Marine Chemistry* (Vol. 5, pp. 3–80). John Wiley & Sons, Inc.

Morel, A., & Berthon, J. (1989). Surface pigments, algal biomass profiles, and potential production of the euphotic layer: Relationships reinvestigated in view of remote-sensing applications. *Limnology and Oceanography*, *34*(8), 1545–1562. https://doi.org/10.4319/lo.1989.34.8.1545

Murnane, R. J. (1994). Determination of thorium and particulate matter cycling parameters at station P: A reanalysis and comparison of least squares techniques. *Journal of Geophysical Research*, *99*(C2), 3393–3405. https://doi.org/10.1029/93JC03155

Murnane, R. J., Cochran, J., Buesseler, K., & Bacon, M. (1996). Least-squares estimates of thorium, particle, and nutrient cycling rate constants from the JGOFS North Atlantic Bloom Experiment. *Deep Sea Research Part I: Oceanographic Research Papers*, *43*(2), 239–258. https://doi.org/10.1016/0967-0637(96)00004-0

Murnane, R. J., Cochran, J. K., & Sarmiento, J. L. (1994). Estimates of particle- and thorium-cycling rates in the northwest Atlantic Ocean. *Journal of Geophysical Research*, *99*(C2), 3373–3392. https://doi.org/10.1029/93JC02378

Murnane, R. J., Sarmiento, J. L., & Bacon, M. P. (1990). Thorium isotopes, particle cycling models, and inverse calculations of model rate constants. *Journal of Geophysical Research*, *95*(C9), 16195–16206. https://doi.org/10.1029/JC095iC09p16195

NASA Ocean Biology Processing Group. (2018). Moderate-resolution Imaging Spectroradiometer (MODIS) Aqua Downwelling Diffuse Attenuation Coefficient Data Version R2018.0 [Dataset]. NASA Ocean Biology DAAC. https://doi.org/10.5067/AQUA/MODIS/L3M/KD/2018

Nguyen, T. T. H., Zakem, E. J., Ebrahimi, A., Schwartzman, J., Caglar, T., Amarnath, K., et al. (2022). Microbes contribute to setting the ocean carbon flux by altering the fate of sinking particulates. *Nature Communications*, *13*(1), 1657. https://doi.org/10.1038/s41467-022-29297-2

Omand, M. M., Steinberg, D. K., & Stamieszkin, K. (2021). Cloud shadows drive vertical migrations of deep-dwelling marine life. *Proceedings of the National Academy of Sciences*, *118*(32). https://doi.org/10.1073/pnas.2022977118

Passow, U. (2002). Transparent exopolymer particles (TEP) in aquatic environments. *Progress in Oceanography*, *55*(3–4), 287–333. https://doi.org/10.1016/S0079-6611(02)00138-6

Paul, N., Bressac, M., Boyd, P. W., & Santoro, A. (2022). Quantifying particle-attached microbial respiration with depth in the Santa Barbara Basin, North Pacific, and North Atlantic. [Oral presentation].

Pavia, F. J., Anderson, R. F., Lam, P. J., Cael, B. B., Vivancos, S. M., Fleisher, M. Q., et al. (2019). Shallow particulate organic carbon regeneration in the South Pacific Ocean. *Proceedings of the National Academy of Sciences*, *116*(20), 9753–9758. https://doi.org/10.1073/pnas.1901863116

Polovina, J. J., Howell, E., Kobayashi, D. R., & Seki, M. P. (2001). The transition zone chlorophyll front, a dynamic global feature defining migration and forage habitat for marine resources. *Progress in Oceanography*, *49*(1–4), 469–483. https://doi.org/10.1016/S0079-6611(01)00036-2

Rutgers van der Loeff, M. M., & Berger, G. W. (1993). Scavenging of 230Th and 231Pa near the antarctic polar front in the South Atlantic. *Deep Sea Research Part I: Oceanographic Research Papers*, *40*(2), 339–357. https://doi.org/10.1016/0967-0637(93)90007-P

Scholten, J. C., Rutgers van der Loeff, M. M., & Michel, A. (1995). Distribution of ^{230}Th and ^{231}Pa in the water column in relation to the ventilation of the deep Arctic basins. *Deep Sea Research Part II: Topical Studies in Oceanography*, *42*(6), 1519–1531. https://doi.org/10.1016/0967-0645(95)00052-6

Siegel, D. A., DeVries, T., Cetinić, I., & Bisson, K. M. (2023). Quantifying the ocean's biological pump and its carbon cycle impacts on global scales. *Annual Review of Marine Science*, *15*(1), 329–356. https://doi.org/10.1146/annurev-marine-040722-115226

Steinberg, D. K., & Landry, M. R. (2017). Zooplankton and the ocean carbon cycle. *Annual Review of Marine Science*, *9*(1), 413–444. https://doi.org/10.1146/annurev-marine-010814-015924

Steinberg, D. K., Van Mooy, B. A. S., Buesseler, K. O., Boyd, P. W., Kobari, T., & Karl, D. M. (2008). Bacterial vs. zooplankton control of sinking particle flux in the ocean's twilight zone. *Limnology and Oceanography*, *53*(4), 1327–1338. https://doi.org/10.4319/lo.2008.53.4.1327

Takahashi, K. (1986). Seasonal fluxes of pelagic diatoms in the subarctic Pacific, 1982–1983. *Deep Sea Research Part A. Oceanographic Research Papers*, *33*(9), 1225–1251. https://doi.org/10.1016/0198-0149(86)90022-1

Tarantola, A., & Valette, B. (1982). Generalized nonlinear inverse problems solved using the least squares criterion. *Reviews of Geophysics and Space Physics*, *20*(2), 219–232. https://doi.org/10.1029/RG020i002p00219

Trull, T., Bray, S., Buesseler, K., Lamborg, C., Manganini, S., Moy, C., & Valdes, J. (2008). In situ measurement of mesopelagic particle sinking rates and the control of carbon transfer to the ocean interior during the Vertical Flux in the Global Ocean (VERTIGO) voyages in the North Pacific. *Deep Sea Research Part II: Topical Studies in Oceanography*, *55*(14–15), 1684–1695. https://doi.org/10.1016/j.dsr2.2008.04.021

Uitz, J., Claustre, H., Morel, A., & Hooker, S. B. (2006). Vertical distribution of phytoplankton communities in open ocean: An assessment based on surface chlorophyll. *Journal of Geophysical Research*, *111*(C8), C08005. https://doi.org/10.1029/2005JC003207

Venchiarutti, C., Jeandel, C., & Roy-Barman, M. (2008). Particle dynamics study in the wake of Kerguelen Island using thorium isotopes. *Deep Sea Research Part I: Oceanographic Research Papers*, *55*(10), 1343–1363. https://doi.org/10.1016/j.dsr.2008.05.015

Vidussi, F., Claustre, H., Manca, B. B., Luchetta, A., & Marty, J.-C. (2001). Phytoplankton pigment distribution in relation to upper thermocline circulation in the eastern Mediterranean Sea during winter. *Journal of Geophysical Research*, *106*(C9), 19939–19956. https://doi.org/10.1029/1999JC000308

Villa-Alfageme, M., De Soto, F. C., Ceballos, E., Giering, S. L. C., Le Moigne, F. A. C., Henson, S., et al. (2016). Geographical, seasonal, and depth variation in sinking particle speeds in the North Atlantic: Sinking particle speeds depth variation. *Geophysical Research Letters*, *43*(16), 8609–8616. https://doi.org/10.1002/2016GL069233

Wassmann, P. (1998). Retention versus export food chains: Processes controlling sinking loss from marine pelagic systems. *Hydrobiologia*, 29–57. https://doi.org/10.1007/978-94-017-1493-8_3

Westberry, T., Behrenfeld, M. J., Siegel, D. A., & Boss, E. (2008). Carbon-based primary productivity modeling with vertically resolved photoacclimation. *Global Biogeochemical Cycles*, *22*(2), GB2024. https://doi.org/10.1029/2007GB003078

Wurl, O., Miller, L., & Vagle, S. (2011). Production and fate of transparent exopolymer particles in the ocean. *Journal of Geophysical Research*, *116*(C7), C00H13. https://doi.org/10.1029/2011JC007342

Xiang, Y., & Lam, P. J. (2020). Size-fractionated compositions of Marine suspended particles in the Western Arctic Ocean: Lateral and Vertical sources. *Journal of Geophysical Research: Oceans*, *125*(8), e2020JC016144. https://doi.org/10.1029/2020JC016144

Xiang, Y., Lam, P. J., Burd, A. B., & Hayes, C. T. (2022). Estimating mass flux from size-fractionated filtered particles: Insights into controls on sinking velocities and mass fluxes in recent U.S. GEOTRACES cruises. *Global Biogeochemical Cycles*, *36*(4), e2021GB007292. https://doi.org/10.1029/2021GB007292

Yamamoto, A., Abe-Ouchi, A., & Yamanaka, Y. (2018). Long-term response of oceanic carbon uptake to global warming via physical and biological pumps. *Biogeosciences*, *15*(13), 4163–4180. https://doi.org/10.5194/bg-15-4163-2018

Zamanillo, M., Ortega-Retuerta, E., Nunes, S., Rodríguez-Ros, P., Dall'Osto, M., Estrada, M., et al. (2019). Main drivers of transparent exopolymer particle distribution across the surface Atlantic Ocean. *Biogeosciences*, *16*(3), 733–749. https://doi.org/10.5194/bg-16-733-2019